

THE TIME-RESOLVED SPECTRA OF PHOTOSPHERIC EMISSION FROM A STRUCTURED JET FOR GAMMA-RAY BURSTS

YAN-ZHI MENG^{1,2}, LIANG-DUAN LIU^{3,4}, JUN-JIE WEI¹, XUE-FENG WU¹, BIN-BIN ZHANG^{3,4}

¹Purple Mountain Observatory, Chinese Academy of Sciences, Nanjing 210008, China; xfwu@pmo.ac.cn

²University of Chinese Academy of Sciences, Beijing 100049, China

³School of Astronomy and Space Science, Nanjing University, Nanjing 210093, China and

⁴Key Laboratory of Modern Astronomy and Astrophysics (Nanjing University), Ministry of Education, China

Draft version September 2, 2019

ABSTRACT

The quasi-thermal components found in many *Fermi* gamma-ray bursts (GRBs) imply that the photosphere emission indeed contributes to the prompt emission of many GRBs. But whether the observed spectra empirically fitted by the Band function or cutoff power law, especially the spectral and peak energy (E_p) evolutions can be explained by the photosphere emission model alone needs further discussion. In this work, we investigate in detail the time-resolved spectra and E_p evolutions of photospheric emission from a structured jet, with an inner-constant and outer-decreasing angular Lorentz factor profile. Also, a continuous wind with a time-dependent wind luminosity has been considered. We show that the photosphere spectrum near the peak luminosity is similar to the cutoff power-law spectrum. The spectrum can have the observed average low-energy spectral index $\alpha \sim -1$, and the distribution of the low-energy spectral index in our photosphere model is similar to that observed ($-2 \lesssim \alpha \lesssim 0$). Furthermore, the two kinds of spectral evolutions during the decay phase, separated by the width of the core (θ_c), are consistent with the time-resolved spectral analysis results of several *Fermi* multi-pulse GRBs and single-pulse GRBs, respectively. Also, for this photosphere model we can reproduce the two kinds of observed E_p evolution patterns rather well. Thus, by considering the photospheric emission from a structured jet, we reproduce the observations well for the GRBs best fitted by the cutoff power-law model for the peak-flux spectrum or the time-integrated spectrum.

Subject headings: gamma-ray burst: general – radiation mechanisms: thermal – radiative transfer – scattering

1. INTRODUCTION

After decades of investigations, the radiation mechanism of gamma-ray burst (GRB) prompt emission remains unclear. Optically thin synchrotron emission caused by internal shocks (Rees & Meszaros 1994) has been the most widely discussed model for many years, since it can naturally explain the non-thermal nature of the observed typical spectrum, which is a smoothly joint broken power law called the “Band” function (Band et al. 1993). Observationally, the typical low-energy photon index α of the Band function is around -1 (Preece et al. 2000; Nava et al. 2011; Zhang et al. 2011). However, this model is found to face several difficulties in recent years. First, many of the observed bursts have a harder low-energy slope than the death line $\alpha = -2/3$, which cannot be obtained by basic synchrotron theory (Crider et al. 1997; Preece et al. 1998; Kaneko et al. 2006; Goldstein et al. 2012). Second, the spectral width for a large fraction of GRBs is found so narrow that it cannot be explained by synchrotron radiation (Axelsson & Borgonovo 2015; Yu et al. 2015). Third, the narrow distribution at a few hundred keV of the observed peak energies cannot be well explained. Finally, since only the relative kinetic energy between different shells in the internal shock model can be released, the radiation efficiency is rather low (Kobayashi et al. 1997; Lazzati et al. 1999; Guetta et al. 2001; Kino et al. 2004), which contradicts with the observed high efficiency of a few tens of percent (Fan & Piran 2006;

Zhang et al. 2007; Beniamini et al. 2015).

Due to these difficulties for the internal shock model¹, the photospheric emission model seems to be a promising scenario (e.g., Thompson 1994; Mészáros & Rees 2000; Rees & Mészáros 2005; Pe’er & Ryde 2011; Toma et al. 2011; Fan et al. 2012; Lazzati et al. 2013; Lundman et al. 2013; Ruffini et al. 2013; Deng & Zhang 2014; Bégué & Pe’er 2015; Gao & Zhang 2015; Pe’er et al. 2015; Ryde et al. 2017; Acuner & Ryde 2018; Hou et al. 2018; Meng et al. 2018; Li 2019a). The photospheric emission is the reasonable result of the original fireball model (Goodman 1986; Paczynski 1986), since at the base of the outflow the optical depth is much greater than unity (e.g. Piran 1999). As the fireball expands and becomes transparent, the internally trapped photons are eventually released at the photosphere. The photospheric emission model naturally explains the clustering of the peak energies and the high radiation efficiency observed.

Indeed, a quasi-thermal component has been found in tens of BATSE GRBs (Ryde 2004, 2005; Ryde & Pe’er 2009) and some *Fermi* GRBs (GRB 090902B, Abdo et al. 2009, Ryde et al. 2010, Zhang 2011; GRB100724B, Guiriec et al. 2011; GRB 110721A, Axelsson et al. 2012; GRB 100507, Ghirlanda et al. 2013; GRB 101219B, Larsson et al. 2015; and the

¹ Some scenarios within the synchrotron radiation model have been proposed to alleviate these difficulties (e.g., Zhang & Yan 2011; Geng et al. 2018a).

short GRB 120323A, Guiriec et al. 2013). Especially in the case of GRB 090902B, the photospheric emission dominates the observed emission. But whether the whole observed Band function or cutoff power law is of a photosphere origin remains unknown. If they are, the quasi-thermal spectrum needs to be broadened. Two different ways of broadening have been considered currently: subphotospheric dissipation (Rees & Mészáros 2005; Giannios 2006; Beloborodov 2017; Vurm & Beloborodov 2016) and geometric broadening (Pe’er 2008; Ito et al. 2013; Lundman et al. 2013; Deng & Zhang 2014).

Generally, photosphere is defined as a surface where the Thompson scattering optical depth τ for a photon is $\tau = 1$. Consistent with Abramowicz et al. (1991), Pe’er (2008) found that the photospheric radius R_{ph} is angle-dependent for a relativistic, spherically symmetric wind, $R_{\text{ph}}(\theta) \propto (\theta^2/3 + 1/\Gamma^2)$, where θ is the angle measured from the line of sight (LOS) and Γ is the outflow bulk Lorentz factor. But in principle, the photons can be last scattered at any position (r, Ω) inside the outflow, where r is the distance from the explosion center and $\Omega(\theta, \phi)$ is the angular coordinates. Thus, a probability function $P(r, \Omega)$ is brought in to describe the possibility of last scattering at any location (Pe’er 2008; Beloborodov 2011; Pe’er & Ryde 2011). Also, the observed spectrum is a superposition of a collection of blackbodies with different temperature, therefore it is broadened (namely geometric broadening).

Based on the geometric broadening, Deng & Zhang (2014) performed a detailed study of the photosphere emission spectrum for the spherically symmetric wind. They showed that the spectrum below E_p can be modified to $F_\nu \sim \nu^{1.5}$ ($\alpha \sim +0.5$), which is not consistent well with the observation ($\alpha \sim -1.0$). Also, for the E_p evolution as a function of photosphere luminosity, the $L_{\text{ph}} - E_p$ anti-correlation is clearly shown. The observed hard-to-soft evolution and E_p -intensity tracking (Ford et al. 1995; Liang & Kargatis 1996; Ghirlanda et al. 2010; Lu et al. 2010, 2012) cannot be reproduced well. They thus claimed that a more complicated photosphere model may be needed. Here in this work, by considering the photosphere emission for a jet with lateral structure, we show that the observed typical low-energy photon index ($\alpha \sim -1.0$) and E_p evolutions (hard-to-soft evolution or E_p -intensity tracking) can be obtained. Indeed within the collapsar model (MacFadyen & Woosley 1999), as the jet gets through the collapsing progenitor star, the pressure of the surrounding gas collimates it (e.g., Zhang, Woosley & MacFadyen 2003; Morsony, Lazzati & Begelman 2007; Mizuta, Nagataki & Aoi 2011), thus the jet may have angular profiles of energy flux and Lorentz factor, namely a structured jet (e.g., Dai & Gou 2001; Rossi et al. 2002; Zhang & Mészáros 2002; Zhang et al. 2004; Beniamini et al. 2019; Beniamini & Nakar 2019). Noteworthy, this structured jet is well believed to exist in GRB 170817A (the first joint detection of short GRB and gravitational wave, Lazzati et al. 2018; Lyman et al. 2018; Meng et al. 2018; Mooley et al. 2018; Zhang et al. 2018b; Ghirlanda et al. 2019), whose unusual performance of the prompt emission and the afterglow has invoked hot debate (e.g., Ai et al. 2018; Geng et al.

2018b; Li et al. 2018; Lin et al. 2018; Geng et al. 2019; Lan et al. 2019; Li et al. 2019; Wang et al. 2019). Previously, Lundman et al. (2013) showed that, with the collimated and steady-state jet the photospheric spectrum can reproduce the observed average low-energy photon index $\alpha \approx -1$. But for the photospheric emission from a structured jet, the time-resolved spectra, the spectral evolutions, more reasonable energy injection of continuous wind, the effect of variable wind luminosity and the evolution of E_p need to be further explored, which are the main contents in our work.

We calculate the time-resolved photosphere spectra from a structured jet for progressively more reasonable energy injections: impulsive injection, continuous wind with a constant wind luminosity and continuous wind with a variable wind luminosity. We also perform the time-resolved spectral analysis of several GRBs observed by *Fermi* GBM and possessing a pulse that has a rather good profile, and then compare the spectral evolutions of this analysis and the model. In addition, we discuss the luminosity profiles and E_p evolution based on the model calculation. We show that the photosphere spectrum around the peak luminosity is close to the spectrum of the cutoff power-law model, which is the best-fit model for large amounts of the time-resolved spectra in GRBs (e.g., Kaneko et al. 2006; Yu et al. 2016). Also, the spectrum can get a flattened shape ($\alpha \sim -1$) below the peak, and the distribution of the low-energy spectral index is similar to that observed ($-2 \lesssim \alpha \lesssim 0$). Based on the model calculation, the two types of spectral evolutions (decided by the width of the core) during the decay phase are consistent with the time-resolved spectral analysis results of several *Fermi* multi-pulse GRBs and single-pulse GRBs, respectively. Finally, for this photosphere model we can reproduce the two types of observed E_p evolution patterns rather well.

The paper is organized as follows. In Section 2, we describe the basic assumptions in our photosphere model. We then present the calculations of the time-resolved photosphere spectra for progressively more reasonable energy injections, the time-resolved spectral analysis of several *Fermi* GRBs and the discussion on E_p evolution in Section 3. The conclusions are drawn in Section 4.

2. BASIC ASSUMPTIONS

The basic physical picture of our paper is shown in Figure 1. The photons are continuously emitted into a series of layers released by a long-lasting central engine, and the wind luminosity of the central engine is time-dependent, similar to those in Deng & Zhang (2014) (see Figure 1 therein). But in our model, the jet is structured, with an inner-constant and outer-decreasing angular Lorentz factor profile (as seen in Figure 1 of Lundman et al. 2013) and an angle-independent luminosity². The angular Lorentz factor profile takes the form

$$(\Gamma - \Gamma_{\text{min}})^2 = \frac{(\Gamma_0 - \Gamma_{\text{min}})^2}{(\theta/\theta_c)^{2p} + 1}, \quad (1)$$

² As shown in Lundman et al. (2013), for a prompt GRB spectrum the part expected to be observed is formed by the photons making their final scattering at approximately $\lesssim 5/\Gamma_0$, where $dL/d\Omega \approx \text{const}$ (see the top panels of Figures 8 and 9 in Zhang, Woosley & MacFadyen 2003).

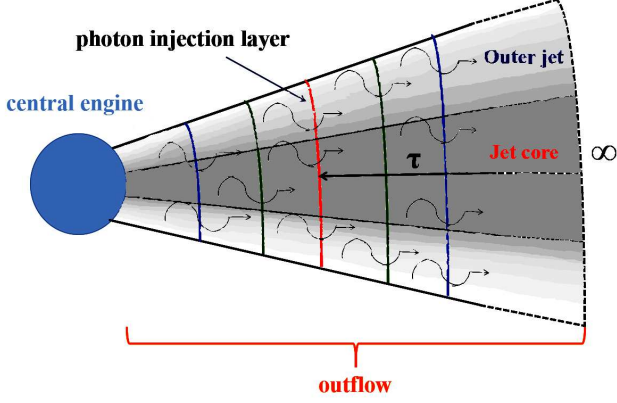


FIG. 1.— Basic picture of our model. Long-lasting central engine with a variable wind luminosity and an inner constant and outer decreased angular Lorentz factor profile are assumed. Different colors of the layers represent different wind luminosity (the maximum for the red, the minimum for the blue). Also, the grayscale in the lateral directions shows the Lorentz factor profile (darker for larger Lorentz factor).

where Γ_0 is the constant Lorentz factor in the jet core, θ_c is the half-opening angle for the jet core, p is the power-law index of the profile, and $\Gamma_{\min} = 1.2$ is the minimum value of the Lorentz factor.

Also, the effect of the non-zero viewing angle (θ_v) is the same as that shown in Figure 2 of Lundman et al. (2013). There are two sets of spherical coordinates in the jet: the spherical coordinates (r, θ, ϕ) with the polar axis parallel to the jet axis of symmetry and the spherical coordinates $(r, \theta_{\text{LOS}}, \phi_{\text{LOS}})$ with the polar axis parallel to the LOS. The radial coordinate (r) is along the axis at an angle θ_{LOS} to the LOS and θ to the jet axis.

3. THE TIME-RESOLVED SPECTRA OF MODEL AND OBSERVATION

In this section, we firstly present calculations of the time-resolved photosphere spectra for progressively more reasonable energy injections, impulsive injection in Section 3.1, continuous wind with a constant wind luminosity in Section 3.2, and continuous wind with a variable wind luminosity in Section 3.3. Then in Section 3.4, we compare them with the time-resolved spectral analysis results of several GRBs observed by *Fermi* GBM and possessing a pulse that has a rather good profile. Finally, discussions on the luminosity profiles and E_p evolution patterns are presented in Section 3.5.

3.1. Impulsive Injection

In this section, to calculate the time-resolved spectra, we modify Equation (10) in Lundman et al. (2013) which calculates the time-integrated photospheric spectrum:

$$F_E^{\text{ob}}(\theta_v) = \frac{1}{4\pi d_L^2} \iint (1 + \beta) D^2 \frac{d\dot{N}_\gamma}{d\Omega} \times \frac{R_{\text{dcp}}}{r^2} \exp\left(-\frac{R_{\text{ph}}}{r}\right) \times \left\{ E \frac{dP}{dE} \right\} d\Omega dr, \quad (2)$$

where both the velocity β and the Doppler factor $D = [\Gamma(1 - \beta \cos \theta_{\text{LOS}})]^{-1}$ depend on the angle θ to the jet axis of symmetry [$\beta = \beta(\theta)$, $D = D(\theta, \theta_{\text{LOS}})$]. θ_{LOS} is the angle to the LOS. While the viewing angle θ_v is the angle of the jet axis of symmetry to the LOS. If $\theta_v = 0$,

then $\theta = \theta_{\text{LOS}}$. Else if $\theta_v > 0$, we have

$$\begin{aligned} \theta &= \theta(\theta_{\text{LOS}}, \phi_{\text{LOS}}) \\ &= \arccos[\cos(\theta_{\text{LOS}}) \cos(\theta_v) + \sin(\theta_{\text{LOS}}) \sin(\theta_v) \cos \phi_{\text{LOS}}]. \end{aligned} \quad (3)$$

Thus, $\beta(\theta_{\text{LOS}}, \phi_{\text{LOS}}) = \beta[\theta(\theta_{\text{LOS}}, \phi_{\text{LOS}})]$ and $D(\theta_{\text{LOS}}, \phi_{\text{LOS}}) = D[\theta(\theta_{\text{LOS}}, \phi_{\text{LOS}}), \theta_{\text{LOS}}]$.

Since the outflow luminosity is assumed to be angle-independent, the photon emission rate at the base of the outflow, $r = r_0$, is also independent of angle, $d\dot{N}_\gamma/d\Omega = \dot{N}_\gamma/4\pi$ and $\dot{N}_\gamma = L/2.7k_B T_0$, where L is the total outflow luminosity and $T_0 = (L/4\pi r_0^2 a c)^{1/4}$ is the base outflow temperature.

The decoupling radius, R_{dcp} , is defined as the radius where the optical depth to scattering a photon moving in the radial direction becomes unity. While the photospheric radius, R_{ph} , is the radius where the optical depth to scattering a photon moving towards the observer becomes unity. Their difference is the direction where the photon propagates.

The decoupling radius, R_{dcp} , can be calculated by

$$R_{\text{dcp}} = \frac{1}{(1 + \beta)\beta\Gamma^2} \frac{\sigma_T}{m_p c} \frac{d\dot{M}}{d\Omega}, \quad (4)$$

where $d\dot{M}(\theta)/d\Omega = L/4\pi c^2 \Gamma(\theta)$ is the angle-dependent mass outflow rate per solid angle. Thus, the decoupling radius is also angle-dependent.

While the photospheric radius, R_{ph} , can be written as

$$R_{\text{ph}} = \frac{\sigma_T}{m_p c \sin \theta_{\text{LOS}}} \int_0^{\theta_{\text{LOS}}} \frac{(1 - \beta \cos \tilde{\theta}_{\text{LOS}})}{\beta} \frac{d\dot{M}}{d\tilde{\Omega}} d\tilde{\theta}_{\text{LOS}}. \quad (5)$$

In the former term of Equation (2), $[(1 + \beta)D^2/4\pi] \cdot (R_{\text{dcp}}/r^2) \exp(-R_{\text{ph}}/r)$ represents the probability density function for the final scattering to happen at the radius r and the angular coordinate $\Omega(\theta, \phi)$, namely, $P(r, \Omega)$. Also, this term is very similar to the probability density function used in Pe'er & Ryde (2011) and that introduced in Beloborodov (2011).

For the latter term $E \cdot (dP/dE)$, dP/dE describes the probability for a photon to have an observer frame energy

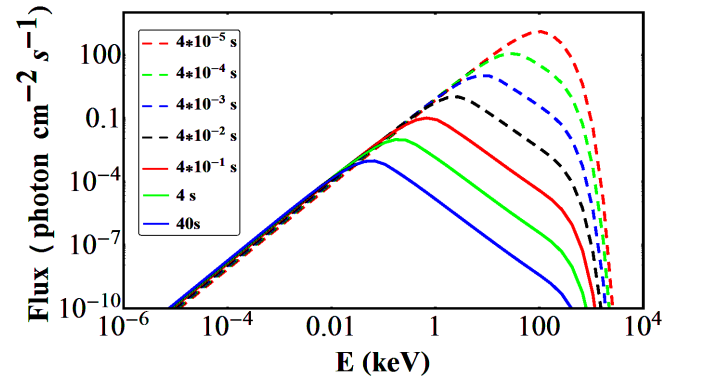


FIG. 2.— Instantaneous photosphere spectra from a structural jet with impulsive injection of energy. The Lorentz factor profile $\Gamma_0 = 400$, $\theta_c \Gamma_0 = 1$ and $p = 1$ is used along with $\theta_v = 0$. A total outflow luminosity of $L = 10^{52}$ erg s^{-1} is assumed, base outflow radius $r_0 = 10^8$ cm, and luminosity distance $d_L = 4.85 \times 10^{28}$ cm ($z = 2$). Different line styles represent different observational times.

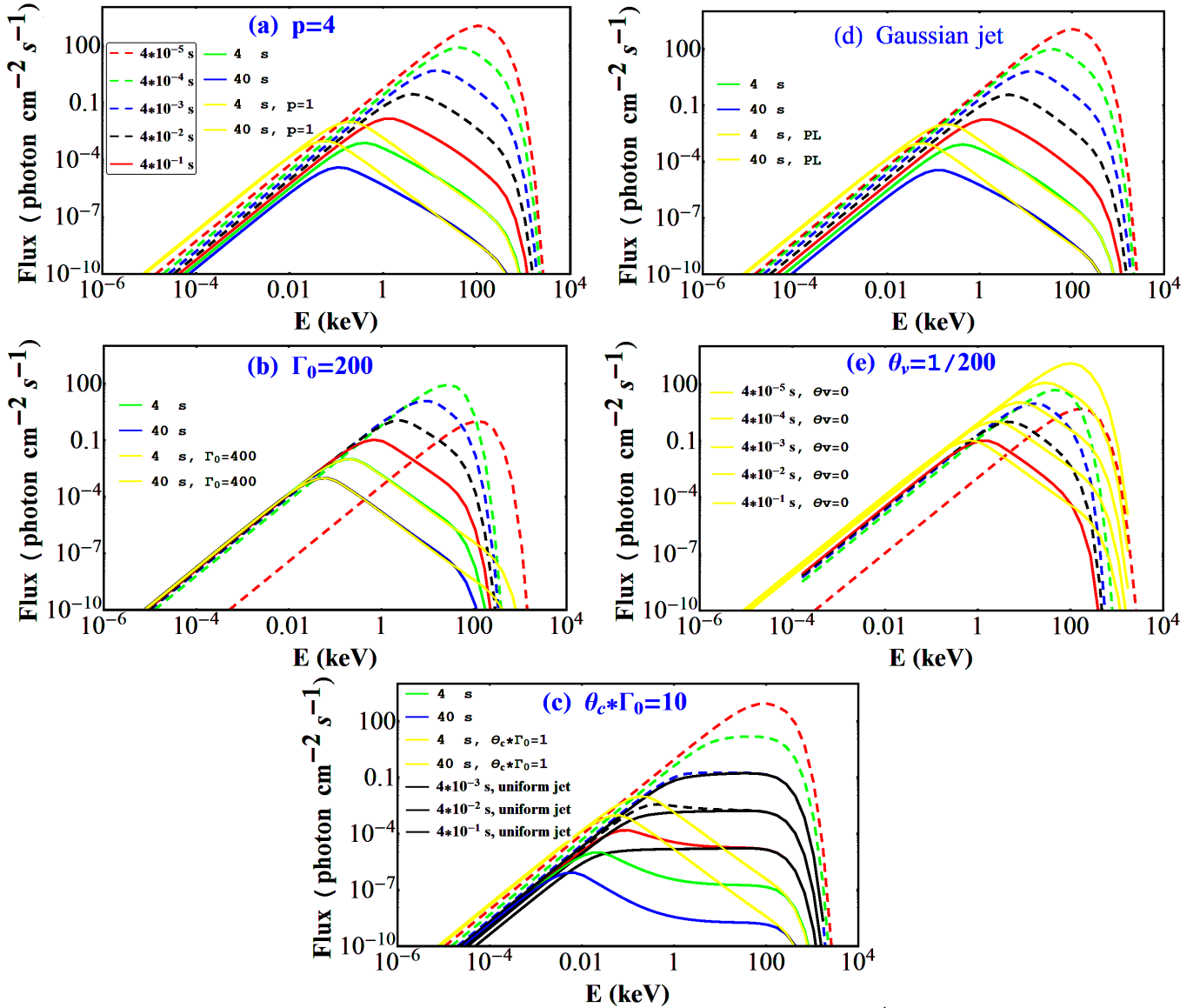


FIG. 3.— Time-resolved spectra for different Lorentz factor profiles or viewing angle. (a) A larger Lorentz factor gradient $p = 4$, along with $\Gamma_0 = 400$, $\theta_c \Gamma_0 = 1$ and $\theta_v = 0$. (b) $\Gamma_0 = 200$, with $\theta_c = 1/\Gamma_0$, $p = 1$ and $\theta_v = 0$. (c) A wider jet core $\theta_c = 10/\Gamma_0 = 1/40$, with $\Gamma_0 = 400$, $p = 1$ and $\theta_v = 0$. (d) Gaussian jet with $\Gamma_0 = 400$, $\theta_c = 1/400$, and $\theta_v = 0$. (e) Non-zero viewing angle $\theta_v = 1/200$, with $\Gamma_0 = 400$, $\theta_c = 1/400$ and $p = 1$. The yellow spectra in each figure represent the spectra of the corresponding time in Figure 2. While the black solid spectra in Figure 3c are for the uniform jet. Note that the line styles and the corresponding observational times within the box in Figure 3a are applied to all the figures (from 3a to 3e).

between E and $E + dE$ within volume element dV . It is derived as

$$\frac{dP}{dE} = \frac{1}{2.40(k_B T^{\text{ob}})^3} \frac{E^2}{\exp(E/k_B T^{\text{ob}}) - 1}, \quad (6)$$

where $T^{\text{ob}}(r, \Omega) = D(\Omega) \cdot T'(r, \Omega)$ is the observer frame temperature, $T'(r, \Omega)$ is the comoving temperature. Notice that the comoving temperature also depends on the angle, since the Lorentz factor Γ , the saturation radius R_s and the photospheric radius R_{ph} are all angle-

dependent, i.e.,

$$T'(r, \Omega) = \begin{cases} \frac{T_0}{\Gamma(\Omega)}, & r < R_s(\Omega) < R_{\text{ph}}(\Omega), \\ \frac{T_0 [r/R_s(\Omega)]^{-2/3}}{\Gamma(\Omega)}, & R_s(\Omega) < r < R_{\text{ph}}(\Omega), \\ \frac{T_0 [R_{\text{ph}}(\Omega)/R_s(\Omega)]^{-2/3}}{\Gamma(\Omega)}, & R_s(\Omega) < R_{\text{ph}}(\Omega) < r. \end{cases} \quad (7)$$

Adding a δ -function $\delta(t - ru/\beta c)$ to Equation (2), $u = (1 - \beta \cos \theta_{\text{LOS}})$ here, we get the formula that calculates the instantaneous spectrum at the observer time t :

$$F_E^{\text{ob}}(\theta_v, t) = \frac{1}{4\pi d_L^2} \iint (1 + \beta) D^2 \frac{d\dot{N}_\gamma}{d\Omega} \times \frac{R_{\text{dcp}}}{r^2} \exp\left(-\frac{R_{\text{ph}}}{r}\right) \left\{ E \frac{dP}{dE} \right\} \times \delta\left(t - \frac{ru}{\beta c}\right) d\Omega dr. \quad (8)$$

Since $\beta c/u$ is independent of t , we have $\delta(t - ru/\beta c) = (\beta c/u) \times \delta(r = \beta ct/u)$. Meanwhile, taking into account the effect of redshift, we have

$$F_{E^{\text{ob}}}^{\text{ob}}(\theta_v, t) = \frac{1}{4\pi d_L^2} \int (1 + \beta) D^2 \frac{d\dot{N}_\gamma}{d\Omega} \times \frac{R_{\text{dcp}}}{r^2} \exp\left(-\frac{R_{\text{ph}}}{r}\right) \left\{ E \frac{dP}{dE} \right\} \times \frac{\beta c}{u} d\Omega, \quad r = \frac{\beta ct}{u}, \quad E = (1 + z)E^{\text{ob}}. \quad (9)$$

So, through the numerical integration of Equation (9), we obtain the time-resolved spectra. The results are presented in Figs 2 and 3. We have considered a big set of the parameter space region: $\Gamma_0 = 200, 400$; $p = 1, 4$; $\theta_c \Gamma_0 = 1, 10$ and $\theta_v/\theta_c = 0, 2$. The Gaussian jet is considered, too. Also, a total outflow luminosity of $L = 10^{52}$ erg s^{-1} and the base outflow radius $r_0 = 10^8$ cm are assumed. A luminosity distance of $d_L = 4.85 \times 10^{28}$ cm ($z = 2$, which is the peak of the GRB formation rate according to Pescalli et al. 2016) is used for spectrum normalization and redshift effect.

In Figure 2, we consider a narrow jet core ($\theta_c = 1/\Gamma_0$) with the Lorentz factor gradient $p = 1$ observed at $\theta_v = 0$. Obviously, in this case the time-resolved photosphere spectrum evolves from the pure blackbody (early on) to a power law with negative index ($F_\nu \sim \nu^{-1.75}$). The late-time spectrum is quite different from the flattened shape for the uniform jet (Pe'er & Ryde 2011; Deng & Zhang 2014). In addition, the power law has an exponential tail of blackbody emission at the high-energy end, which is the same as the case of the uniform jet.

From Figure 3, we can compare the spectral evolutions for different Lorentz factor profiles or viewing angle. As shown in Figure 3a, with a larger Lorentz factor gradient $p = 4$, the late-time power law is more flat. This is because that the outer jet region becomes more narrow and thus contributes less to the spectra. Also, Figure 3d is quite similar to Figure 3a, because the Lorentz factor falls down very quickly for the Gaussian profile, too. For $p = 4$, when $\Gamma \sim 1$, we have $\theta \sim (\Gamma_0/1)^{1/4} \cdot \theta_c \sim 4.5\theta_c$; while for Gaussian jet, $\theta \sim \sqrt{2 \ln(\Gamma_0/1)} \cdot \theta_c \sim 3.5\theta_c$. Figure 3b shows that, when Γ_0 is smaller the slope of the power law has no change, but the cut-off energy on the high-energy end decreases. Surely the peak energy of the early-time blackbody decreases too, and the blackbody arrives later. Furthermore, Figure 3e is close to Figure 3b, which means if the viewing angle is non-zero the spectral evolution is similar. Finally, Figure 3c presents the time-resolved spectra for a wider jet core $\theta_c = 10/\Gamma_0$. Compared with the yellow spectra (for the narrow jet core), we find that the late-time power law flattens significantly, but not completely (compared with the black solid spectra for the uniform jet).

3.2. Continuous Wind with a Constant Wind Luminosity

GRBs are observed to have a duration, we thus consider the more reasonable case that the central engine produces a continuous wind. In this section, the wind luminosity and the baryon loading rate at different time are assumed to be constant, thus the Lorentz factor is

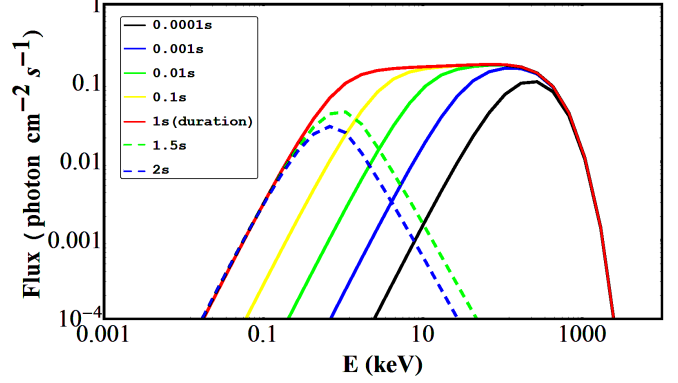


FIG. 4.— Time-resolved photosphere spectra for the continuous wind with abrupt shut-down at 1 s (red). The parameters are the same as Figure 2.

also constant:

$$\begin{aligned} L_w(\hat{t}) &= L_0, \\ \dot{M}(\hat{t}) &= \dot{M}_0, \\ \eta(\hat{t}) &= \Gamma(\hat{t}) = \Gamma(\hat{t} = 0), \end{aligned} \quad (10)$$

where \hat{t} indicates the central-engine time since the very first layer of the wind was injected.

We may consider that the wind consists of many thin layers, with each layer indicated by its injection time \hat{t} . For a layer ejected from \hat{t} to $\hat{t} + d\hat{t}$, the spectrum at the observer time t (for $t > \hat{t}$) is

$$F_{E^{\text{ob}}}^{\text{ob}}(\theta_v, t, \hat{t}) = \frac{1}{4\pi d_L^2} \int (1 + \beta) D^2 \frac{d\dot{N}_\gamma}{d\Omega} \times \frac{R_{\text{dcp}}}{r^2} \exp\left(-\frac{R_{\text{ph}}}{r}\right) \left\{ E \frac{dP}{dE} \right\} \times \frac{\beta c}{u} d\Omega, \quad r = \frac{\beta c(t - \hat{t})}{u}, \quad E = (1 + z)E^{\text{ob}}. \quad (11)$$

Compared with Equation (9), the only difference is $r = \beta c(t - \hat{t})/u$. Then, by integrating over all the layers, we get the spectrum at t , i.e.,

$$F_{E^{\text{ob}}}^{\text{ob}}(\theta_v, t) = \int_0^t F_{E^{\text{ob}}}^{\text{ob}}(\theta_v, t, \hat{t}) d\hat{t}. \quad (12)$$

Figure 4 presents the time-resolved photosphere spectra of the continuous wind with time-independent luminosity and Lorentz factor (before 1 s), and the spectral evolution after an abrupt shut-down (at 1 s). Here, we take the same parameters as Figure 2. Before 1 s, the spectrum evolves from a pure blackbody ($t = 10^{-4}$ s) to the spectrum with a flattened shape ($F_\nu \sim \nu^0$) below the peak. This is caused by the superposition of emission from all layers, since the spectrum from the old layer is a power law with negative index ($F_\nu \sim \nu^{-1.75}$) as shown in Figure 2. The flattened shape ($F_\nu \sim \nu^0$) below the peak is consistent with the average low-energy spectral index for the time-resolved spectra observed in GRBs (e.g., Kaneko et al. 2006; Yu et al. 2016). After an abrupt shut-down (at 1 s) the power law with negative index shows up quickly, but the flux is predominantly low, meaning that there is a rapid falling phase (see the

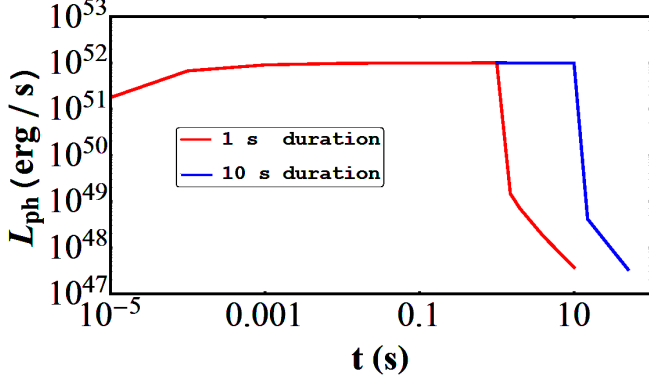


FIG. 5.— Photosphere luminosity light curves of continuous winds, which shut down at 1 s (red) and 10 s (blue). After the shut-down, the light curves fall quickly before entering the t^{-2} phase.

photosphere luminosity light curves in Figure 5). This is the same as the case of the uniform jet.

3.3. Continuous Wind with a Variable Wind Luminosity

Since the light curves of the GRBs show relatively slow change in luminosity, unlike the steep rise and fall (almost within 10^{-4} s) for the case of constant wind luminosity, the wind luminosity may vary with time, rising and then falling gradually.

3.3.1. Wind Luminosity History

Generally, GRB pulses can be fitted well with the exponential model (Norris et al. 2005) or the smoothly joint broken power law model (Kocevski et al. 2003). So, we approximate the wind luminosity history with the broken power law model and the exponential model, respectively.

For the broken power law model, the rising and decaying indices are a_r and a_d respectively, along with a peak luminosity $L_{w,p}$ at \hat{t}_p . Then in the rising phase ($\hat{t} < \hat{t}_p$), the luminosity history can be written as

$$\log L_w(\hat{t}) = a_r \log \hat{t} + b_r, \quad (13)$$

while in the decaying phase ($\hat{t} > \hat{t}_p$), as

$$\log L_w(\hat{t}) = a_d \log \hat{t} + b_d, \quad (14)$$

where $b_r = \log L_{w,p} - a_r \log \hat{t}_p$ and $b_d = \log L_{w,p} - a_d \log \hat{t}_p$ are normalization parameters.

For the exponential model, the luminosity history can be

$$L_w(\hat{t} > \hat{t}_s) = L_{w,p} \times \exp \left[2(\tau_1/\tau_2)^{1/2} \right] \times \exp \left(-\frac{\tau_1}{\hat{t} - \hat{t}_s} - \frac{\hat{t} - \hat{t}_s}{\tau_2} \right), \quad (15)$$

where \hat{t}_s is the start time, τ_1 and τ_2 are respectively the characteristic time scales indicating the rise and decay periods, $L_{w,p}$ is still the peak of luminosity at \hat{t}_p , and $\hat{t}_p = \hat{t}_s + (\tau_1 \cdot \tau_2)^{1/2}$.

3.3.2. Spectra Calculation

From Equation (4), we have $R_{\text{dcp}} \propto L_w^3$. In addition, $R_s = \Gamma r_0$ is independent of L_w . So we normally have $R_{\text{dcp}} \geq R_s$ for a relatively large L_w ($L_w = 10^{52}$ erg s $^{-1}$); but as the wind luminosity may rise and then fall, we may have $R_{\text{dcp}} < R_s$ in the relatively early and late periods of the pulse. In the following, we deal with these two cases, respectively.

$R_{\text{dcp}} \geq R_s$ Case— Since the outflow luminosity varies with time, $d\dot{N}_\gamma/d\Omega$ is surely time-dependent,

$$\frac{d\dot{N}_\gamma(\hat{t})}{d\Omega} = \frac{\dot{N}_\gamma(\hat{t})}{4\pi},$$

$$\dot{N}_\gamma(\hat{t}) = \frac{L_w(\hat{t})}{2.7k_B T_0(\hat{t})}, \quad T_0(\hat{t}) = \left(\frac{L_w(\hat{t})}{4\pi r_0^2 a c} \right)^{1/4}. \quad (16)$$

Note that T_0 is time-dependent, too.

When calculating the decoupling radius R_{dcp} , the optical depth can be written as

$$\tau = \frac{1}{(1+\beta)\beta\Gamma^2} \frac{\sigma_T}{m_p c} \int_{R_{\text{dcp}}}^{\infty} \frac{d\dot{M}}{d\Omega} \frac{1}{r^2} dr. \quad (17)$$

Here, $d\dot{M}(\theta)/d\Omega$ should depend both on \hat{t} and r ($r > R_{\text{dcp}}$). Also, $d\dot{M}/d\Omega$ and Γ are both angle-dependent. We omit writing angular dependences here and below for clarity. $d\dot{M}(\hat{t}, R_{\text{dcp}})/d\Omega = d\dot{M}(\hat{t})/d\Omega = L_w(\hat{t})/4\pi c^2 \Gamma$ is the mass outflow rate at the central engine time \hat{t} , while

$$\frac{d\dot{M}(\hat{t}, r)}{d\Omega} = \frac{L_w(\hat{t} - \Delta\hat{t})}{4\pi c^2 \Gamma} \quad (18)$$

denotes the mass outflow rate at $\hat{t} - \Delta\hat{t}$ (much earlier than \hat{t}), $\Delta\hat{t} = (r - R_{\text{dcp}})/2\Gamma^2\beta c$. In addition, since $\tau \sim 1/r$, we can set the upper limit in Equation (17) as $11R_{\text{dcp}}$. Then, for $L_w = 10^{52}$ erg s $^{-1}$ and $\Gamma = 200$, $\Delta\hat{t} = 10(R_{\text{dcp}}/2\Gamma^2\beta c) \sim 3 \times 10^{-3}$ s \ll 1 s. Thus, we may consider $d\dot{M}/d\Omega$ to be independent of r , which means

$$R_{\text{dcp}}(\hat{t}) = \frac{1}{(1+\beta)\beta\Gamma^2} \frac{\sigma_T}{m_p c} \frac{d\dot{M}(\hat{t})}{d\Omega}. \quad (19)$$

And the other way round, when the photon emitted from the layer (\hat{t}) catches up with the only slightly earlier layer ($\hat{t} - \Delta\hat{t}$, $\Delta\hat{t} \sim 3 \times 10^{-3}$ s), it has reached a quite large radius $11R_{\text{dcp}}$. This means that the assumption of infinity outer boundary is reasonable.

For the same reason, we take $d\dot{M}(\hat{t}, r)/d\Omega \simeq d\dot{M}(\hat{t}, R_{\text{ph}})/d\Omega = d\dot{M}(\hat{t})/d\Omega$ ($r > R_{\text{ph}}$), regardless of the angle-dependent $\Delta\hat{t}$. Thus, the time-dependent photospheric radius $R_{\text{ph}}(\hat{t})$ can be written as

$$R_{\text{ph}}(\hat{t}) = \frac{\sigma_T}{m_p c \sin \theta_{\text{LOS}}} \int_0^{\theta_{\text{LOS}}} \frac{1 - \beta \cos \tilde{\theta}_{\text{LOS}}}{\beta} \frac{d\dot{M}(\hat{t})}{d\Omega} d\tilde{\theta}_{\text{LOS}}. \quad (20)$$

³ As shown in Figure 4 in Lundman et al. (2013), $R_{\text{ph}} \sim R_{\text{dcp}}$. Thus, we only use R_{dcp} to judge how large L_w is.

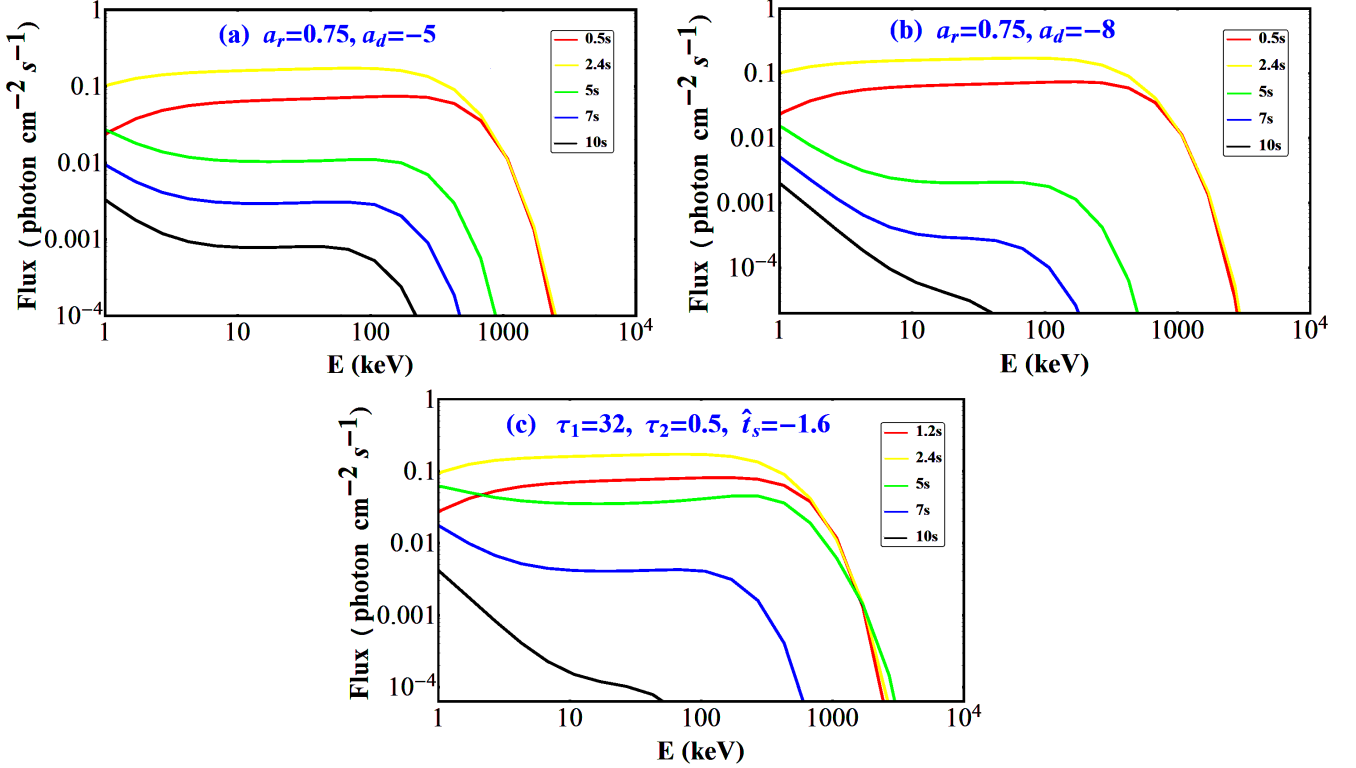


FIG. 6.— Time-resolved spectra of winds with variable luminosity for different luminosity histories. A peak time $\hat{t}_p = 2.4$ s and a peak luminosity $L_{w,p} = 10^{52}$ erg s^{-1} are adopted for all cases. (a) The broken power law model with $a_r = 0.75$ and $a_d = -5$. (b) The broken power law model with $a_r = 0.75$ and $a_d = -8$. (c) The exponential model with $\tau_1 = 32$, $\tau_2 = 0.5$ and $\hat{t}_s = -1.6$. The other parameters are the same as Figure 2. The Lorentz factor profile $\Gamma_0 = 400$, $\theta_c \Gamma_0 = 1$ and $p = 1$ is used along with $\theta_v = 0$. The base outflow radius $r_0 = 10^8$ cm is assumed, and luminosity distance $d_L = 4.85 \times 10^{28}$ cm ($z = 2$). Different colors represent different observational times.

Then, the comoving temperature $T'(r, \Omega, \hat{t})$ can be obtained by (omitting angular dependences):

$$T'(r, \hat{t}) = \begin{cases} T_0(\hat{t})/\Gamma, & r < R_s < R_{\text{ph}}(\hat{t}), \\ T_0(\hat{t})[r/R_s]^{-2/3}/\Gamma, & R_s < r < R_{\text{ph}}(\hat{t}), \\ T_0(\hat{t})[R_{\text{ph}}(\hat{t})/R_s]^{-2/3}/\Gamma, & R_s < R_{\text{ph}}(\hat{t}) < r. \end{cases} \quad (21)$$

Similar to the case of constant wind luminosity, we have

$$F_{E^{\text{ob}}}^{\text{ob}}(\theta_v, t, \hat{t}) = \frac{1}{4\pi d_L^2} \int (1 + \beta) D^2 \frac{d\dot{N}_\gamma(\hat{t})}{d\Omega} \times \frac{R_{\text{dcp}}(\hat{t})}{r^2} \exp\left(-\frac{R_{\text{ph}}(\hat{t})}{r}\right) \left\{ \frac{1}{2.40} \frac{[E/k_B D T'(r, \hat{t})]^3}{\exp[E/k_B D T'(r, \hat{t})] - 1} \right\} \times \frac{\beta c}{u} d\Omega, \quad (22)$$

$$r = \frac{\beta c(t - \hat{t})}{u}, \quad E = (1 + z)E^{\text{ob}}.$$

Then, using Equation (12) to integrate over all the layers, we get the spectrum at t . Note that we must judge whether we have $R_{\text{dcp}}(\hat{t}) \geq R_s$ for the layer ejected at \hat{t} ; if not, we should calculate as following.

$R_{\text{dcp}} < R_s$ Case— In this condition, $d\dot{N}_\gamma(\hat{t})/d\Omega$ is still calculated by Equation (16). As for the decoupling radius R_{dcp} , we have

$$R_{\text{dcp}}(\hat{t}) = \left[\frac{\sigma_T}{6m_p c} \frac{d\dot{M}(\hat{t})}{d\Omega} r_0^2 \right]^{1/3}. \quad (23)$$

Meanwhile, firstly Γ depends on both r and θ , thus it is hard to calculate $R_{\text{ph}}(\hat{t})$. Secondly, $R_{\text{ph}} \sim R_{\text{dcp}}$ (see

the Figure 4 in Lundman et al. 2013). Thirdly, since $R_{\text{dcp}} < R_s$ the observed temperature is close to T_0 if θ is not too large. While as shown in Lundman et al. (2013), for a prompt GRB spectrum the part expected to be observed is formed by the photons making their final scattering at approximately $\lesssim 5/\Gamma_0$. For simplicity, we take

$$R_{\text{ph}}(\hat{t}) = R_{\text{dcp}}(\hat{t}). \quad (24)$$

Besides, the comoving temperature $T'(r, \hat{t})$ is given by

$$T'(r, \hat{t}) = T_0(\hat{t})/\Gamma(\hat{t}), \quad (25)$$

where $\Gamma(\hat{t}) = R_{\text{dcp}}(\hat{t})/r_0$. Then, $F_{E^{\text{ob}}}^{\text{ob}}(\theta_v, t, \hat{t})$ is still calculated by Equation (22), except that

$$\beta = \beta(\hat{t}) = \{1 - [\Gamma(\hat{t})]^{-2}\}^{1/2},$$

$$D = D(\hat{t}) = \frac{1}{\Gamma(\hat{t})} \frac{1}{1 - \beta(\hat{t}) \cos \theta_{\text{LOS}}}. \quad (26)$$

3.3.3. Results

Figures 6a-6c show the calculated, instantaneous spectra of winds with variable luminosity for different luminosity histories. We fix $\hat{t}_p = 2.4$ s, $L_{w,p} = 10^{52}$ erg s^{-1} , $r_0 = 10^8$ cm and $d_L = 4.85 \times 10^{28}$ cm ($z = 2$), and use the Lorentz factor profile $\Gamma_0 = 400$, $\theta_c \Gamma_0 = 1$, $p = 1$ along with $\theta_v = 0$. We investigate three different luminosity profiles, the broken power law model with $(a_r, a_d) = (0.75, -5)$, $(0.75, -8)$ and the exponential model with $\tau_1 = 32$, $\tau_2 = 0.5$ and $\hat{t}_s = -1.6$. For each plot, different colors show different observational

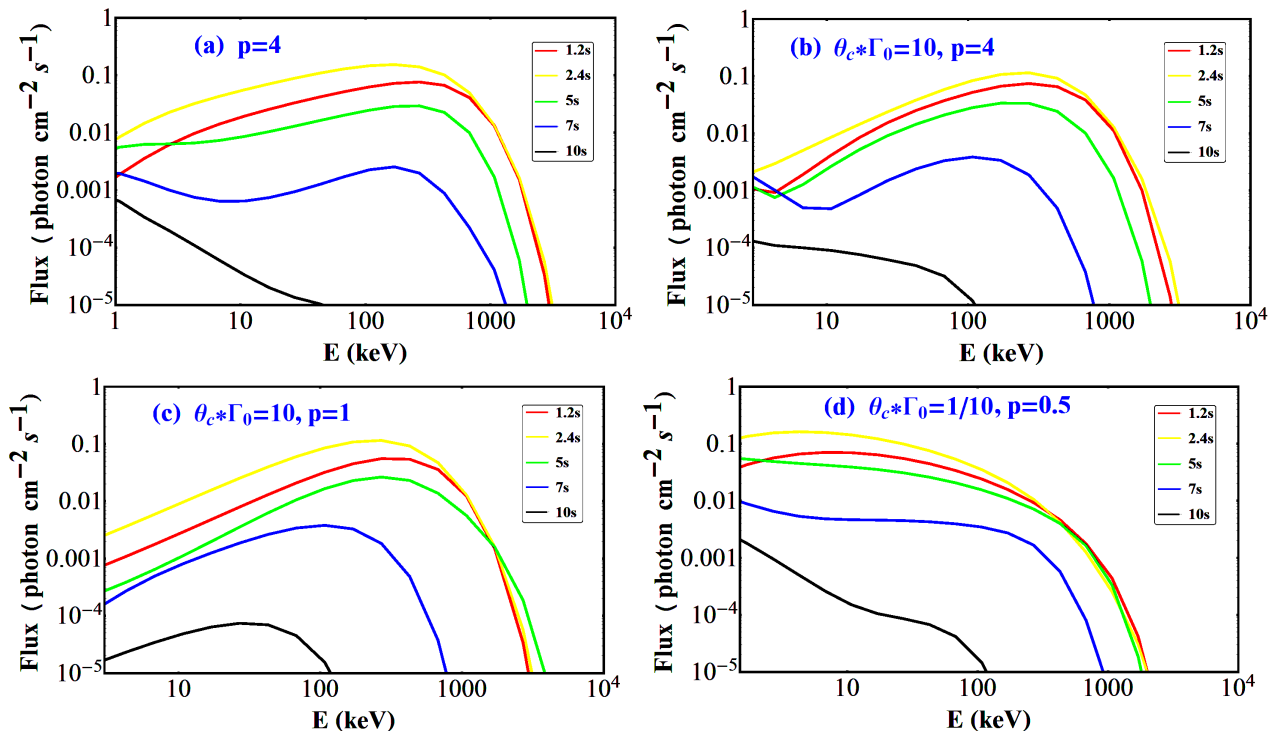


FIG. 7.— Time-resolved spectra of winds with variable luminosity for different Lorentz factor profiles. (a) $p = 4$. (b) $\theta_c \Gamma_0 = 10$, $p = 4$. (c) $\theta_c \Gamma_0 = 10$, $p = 1$. (d) $\theta_c \Gamma_0 = 1/10$, $p = 0.5$. The other parameters are the same as Figure 6c. Different colors represent different observational times.

times. Obviously, during the rising phase ($t = 0.5$ s or 1.2 s, 2.4 s) the resulting spectra are quite similar to those for the case of the constant luminosity (Figure 4), i.e., the spectra have a flattened shape ($F_\nu \sim \nu^0$) below the peak, consistent with the average low-energy spectral index for the time-resolved spectra observed in GRBs (e.g., Kaneko et al. 2006; Yu et al. 2016), and caused by the superposition of emission from the layers injected at different times. During the decay phase ($t = 5$ s, 7 s, 10 s), the power law with negative index shows up gradually. The reason is that the high-latitude emission becomes more dominant (see Figure 2), since it comes from the much earlier layers that have higher luminosities. The steeper the decay phase gets, the more significant the power law with negative index is. For the broken power law model with $(a_r, a_d) = (0.75, -8)$ and the exponential model, the spectrum at $t = 10$ s is fully a power law with negative index.

In Figures 7a-7d, we compare the resulting time-resolved spectra for different Lorentz factor profiles. The other parameters are the same as Figure 6c. As shown in Figure 7a, with a larger Lorentz factor gradient $p = 4$, the resulting spectra during the rising phase ($t = 1.2$ s, 2.4 s) are a little harder ($F_\nu \sim \nu^{0.5}$) below the peak, during the decay phase ($t = 5$ s, 7 s, 10 s), a power law with negative index still shows up gradually. At $t = 7$ s, the spectrum is the mix of a power law with negative index on the low-energy end and a modified blackbody with a shallower low-energy spectral index ($\alpha \sim -0.5$) on the high-energy end. While the spectrum at $t = 10$ s is fully a power law with negative index. Figure 7b presents the time-resolved spectra for a wider jet core with $\theta_c \Gamma_0 = 10$ and $p = 4$, the resulting spectra during the rising phase are similar to Figure 7a, with $F_\nu \sim \nu^{1.0}$ below the peak.

At $t = 7$ s, the spectrum is still the mix of a power law with negative index and a modified blackbody with a shallower low-energy spectral index ($\alpha \sim 0.0$). However, the spectrum at $t = 10$ s is not a power law with negative index, but a modified blackbody with a flattened shape ($F_\nu \sim \nu^0$) below the peak. Figure 7c shows that, with $\theta_c \Gamma_0 = 10$ and $p = 1$, the resulting spectra during the rising phase and the decay phase are almost the same, i.e., a modified blackbody with a shallower low-energy spectral index ($\alpha \sim 0.0$). Finally, Figure 7d presents the time-resolved spectra for a narrower jet core with $\theta_c \Gamma_0 = 1/10$ and $p = 0.5$, the resulting spectra during the rising phase are much softer ($F_\nu \sim \nu^{-0.8}$) below the peak, which is consistent with the lowest low-energy spectral index for the time-resolved spectra observed in GRBs (e.g., Kaneko et al. 2006; Yu et al. 2016). During the decay phase, a power law with negative index shows up gradually also.

Figures 8a-8c show the resulting time-resolved spectra for non-zero viewing angle or smaller Γ_0 . Figure 8a shows that, for a non-zero viewing angle $\theta_v = 1/400$, the resulting spectra during the rising phase are similar to those for $\theta_v = 0$ (see Figure 6c), i.e., the spectra have a flattened shape ($F_\nu \sim \nu^0$) below the peak, but the E_p is much smaller. During the decay phase, the resulting spectra are similar to those for $\theta_v = 0$, too. For $\Gamma_0 = 200$ (smaller), $\theta_c = 1/200$ in Figure 8b and $\theta_c = 1/40$, $p = 4$, $\theta_v = 1/40$ in Figure 8c, the resulting spectra during the rising and decay phases are similar to Figure 8a.

In Figures 9a and 9b, we consider the influence of different r_0 or $L_{w,p}$ on the time-resolved spectra, respectively. For $r_0 = 10^9$ cm and $L_{w,p} = 10^{53}$ erg s $^{-1}$, the resulting spectra during the rising phase change little (compared with Figure 6c). But during the decay phase,

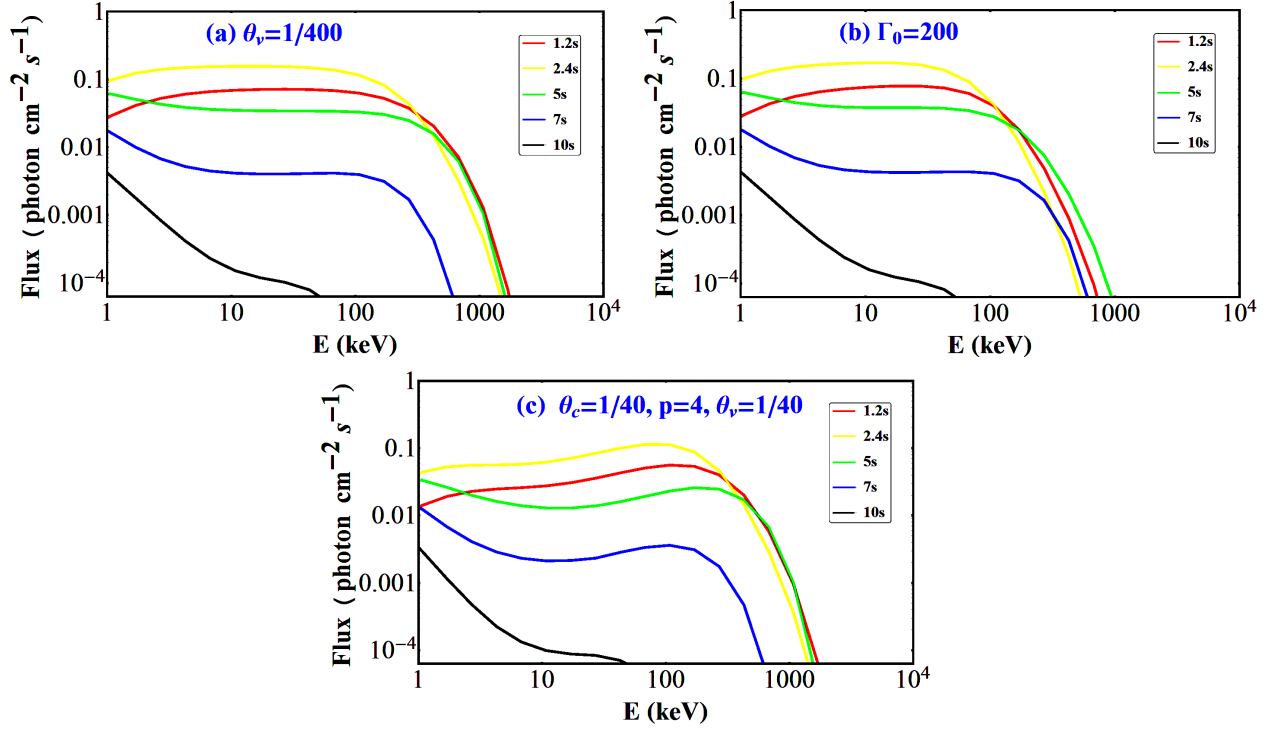


FIG. 8.— Time-resolved spectra of winds with variable luminosity for non-zero viewing angle or smaller Γ_0 . (a) $\theta_v = 1/400$. (b) $\Gamma_0 = 200, \theta_c = 1/200$. (c) $\theta_c = 1/40, p = 4$ and $\theta_v = 1/40$. The other parameters are the same as Figure 6c. Different colors represent different observational times.

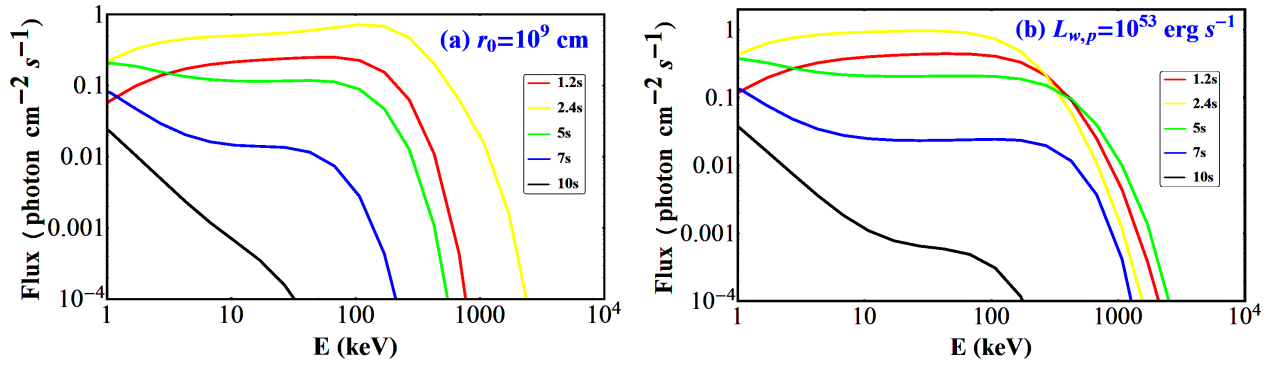


FIG. 9.— Time-resolved spectra of winds with variable luminosity for different r_0 or $L_{w,p}$. (a) $r_0 = 10^9$ cm. (b) $L_{w,p} = 10^{53}$ erg s⁻¹. The other parameters are the same as Figure 6c. Different colors represent different observational times.

the power law with negative index shows up more quickly for $r_0 = 10^9$ cm, while same with Figure 6c for $L_{w,p} = 10^{53}$ erg s $^{-1}$.

3.4. Time-resolved spectral analysis of GRBs observed by *Fermi* GBM

Previously, we calculated the time-resolved spectra of winds with variable luminosity for a big set of the parameter space region. Here, we perform time-resolved spectral analysis of several GRBs observed by *Fermi* GBM and possessing a pulse that has a rather good profile. By comparison, we may know whether the photosphere model with an angular Lorentz factor profile can explain the observed spectral evolution well. We select the GRBs based on Lu et al. (2012), and divide the GRBs into two categories: multi-pulse GRBs (GRB 081125, GRB 090131B and GRB 090626A) which have multiple pulses, and single-pulse GRBs (GRB 081224, GRB 090809B and GRB 110817A) which have single pulse⁴.

3.4.1. multi-pulse GRBs

Figure 10 shows the time-resolved spectral analysis results of GRB 081125. Three different empirical models are fitted to each observed time-resolved spectrum, namely, the Band function (BAND), the cutoff power law (COMP) model and a simple power law (PL). In the top right panel, we present the model spectra of the best-fit models with corresponding parameters for 2.35–2.8 s and 6.3–9.6 s. The spectral fits to the time-resolved spectra for 2.35–2.8 s and 6.3–9.6 s are illustrated in the middle left panel and the bottom right panel, respectively. But we find that neither of the three different empirical models can fit the time-resolved spectra very well for 4.3–5.3 s and 5.3–6.3 s, since the time-resolved spectra seem to be fitted better with the power law model on the low-energy end and the COMP model on the high-energy end. The combined model spectra of the PL plus COMP model with corresponding rough⁵ best-fit parameters are shown in the top right panel also. The observed spectra (fitted with the PL model) for 4.3–5.3 s and 5.3–6.3 s are illustrated in the middle right panel and the bottom left panel, respectively. We find that the observed spectral evolution is quite similar to that for the case of $\theta_c\Gamma_0 = 1$ and $p = 4$ (shown in the top left panel, and same as Figure 7a). The spectra during the rising phase ($t = 1.2$ s, 2.4 s for model, 2.35–2.8 s for observation) are cutoff power law with a little harder than the flattened shape below the peak, during the decay phase ($t = 5$ s, 7 s, 10 s for model, 4.3–5.3 s, 5.3–6.3 s and 6.3–9.6 s for observation), a power law with negative index shows up gradually. At $t = 7$ s for model and 4.3–5.3 s, 5.3–6.3 s for observation, the spectra are all the mix of the power law with negative index on the low-energy end and the modified blackbody with a shallower low-energy spectral index (larger than -1) on the high-energy end. While the spectra at $t = 10$ s for model and 6.3–9.6 s for observation both are fully the power law with negative

⁴ Note that several recent works study the spectral characteristics of the single-pulse dominated GRBs (Yu et al. 2018) and some special multi-pulse GRBs (e.g., Lü et al. 2017; Wei et al. 2017; Zhang et al. 2018a; Li 2019b).

⁵ Since we do not fit the cutoff energy for these two models but fix it at a rough value.

index. Our best-fit results of the time-resolved spectra from GRB 081125 are almost consistent with those of Yu et al. (2016), where the best-fit models before 3.615 s are all the COMP model and the best-fit models after 3.615 s are the PL model.

Similarly, Figure 11 shows the time-resolved spectral analysis results of GRB 090131B. The best-fit results of the time-resolved spectra for several different time intervals are presented in the top right panel. In the bottom panels, the spectral fits to the time-resolved spectra for 24.2–26.6 s (left) and 26.6–30 s (right) are illustrated. The observed spectral evolution is found to be quite similar to that for the case of $\theta_c\Gamma_0 = 1$ and $p = 1$ (shown in the top left panel, and same as Figure 6c). The spectra during the rising phase ($t = 1.2$ s, 2.4 s for model, 22.658–22.907 s, 22.907–23.168 s for observation) are cutoff power law with the flattened shape below the peak, during the decay phase ($t = 5$ s, 7 s, 10 s for model, 23.5–24.2 s, 24.2–26.6 s and 26.6–30 s for observation), a power law with negative index shows up gradually. At $t = 7$ s for model and 23.5–24.2 s for observation, the spectra both are the mix of the power law with negative index on the low-energy end and the modified blackbody with the low-energy flattened shape on the high-energy end. While the spectra at $t = 10$ s for model and 24.2–26.6 s, 26.6–30 s for observation (see the two bottom panels) are all fully the power law with negative index. Our best-fit results of the time-resolved spectra from GRB 090131B are also almost consistent with those of Yu et al. (2016), where the best-fit models before 23.422 s are all the COMP model and the best-fit models after 23.898 s are the PL model.

Also, Figure 12 shows the time-resolved spectral analysis results of GRB 090626A. The best-fit results of the time-resolved spectra for several different time intervals are presented in the left panel, and the spectral fits to the time-resolved spectrum for 8.9–14 s in the right panel. The observed spectral evolution is similar to that for the case of $\theta_c\Gamma_0 = 1$ and $p = 1$ (see Figure 6c), too. And the best-fit results of the time-resolved spectra are also almost consistent with those of Yu et al. (2016), where the best-fit models after 5.888 s are the PL model.

3.4.2. single-pulse GRBs

Figure 13 shows the time-resolved spectral analysis results of GRB 081224. The best-fit results of the time-resolved spectra for several different time intervals are presented in the top right panel. In the bottom panels, the spectral fits to the time-resolved spectra for 2.370–3.037 s (left) and 8.019–13.930 s (right), and the observed spectra (fitted with the PL model) for 5.792–8.019 s (middle) are illustrated. The observed spectral evolution is found to be quite similar to that for the case of $\theta_c\Gamma_0 = 10$ and $p = 4$ (shown in the top left panel, and same as Figure 7b). The spectra during the rising phase ($t = 1.2$ s, 2.4 s for model, 2.370–3.037 s for observation) are still the cutoff power law with a little harder than the flattened shape below the peak. At $t = 7$ s for model and 5.792–8.019 s for observation, the spectra both are the mix of the power law with negative index on the low-energy end and the modified blackbody with a shallower low-energy spectral index (larger than -1) on the high-energy end. However, the spectra at $t = 10$ s for model and 8.019–13.930 s for observation are not the

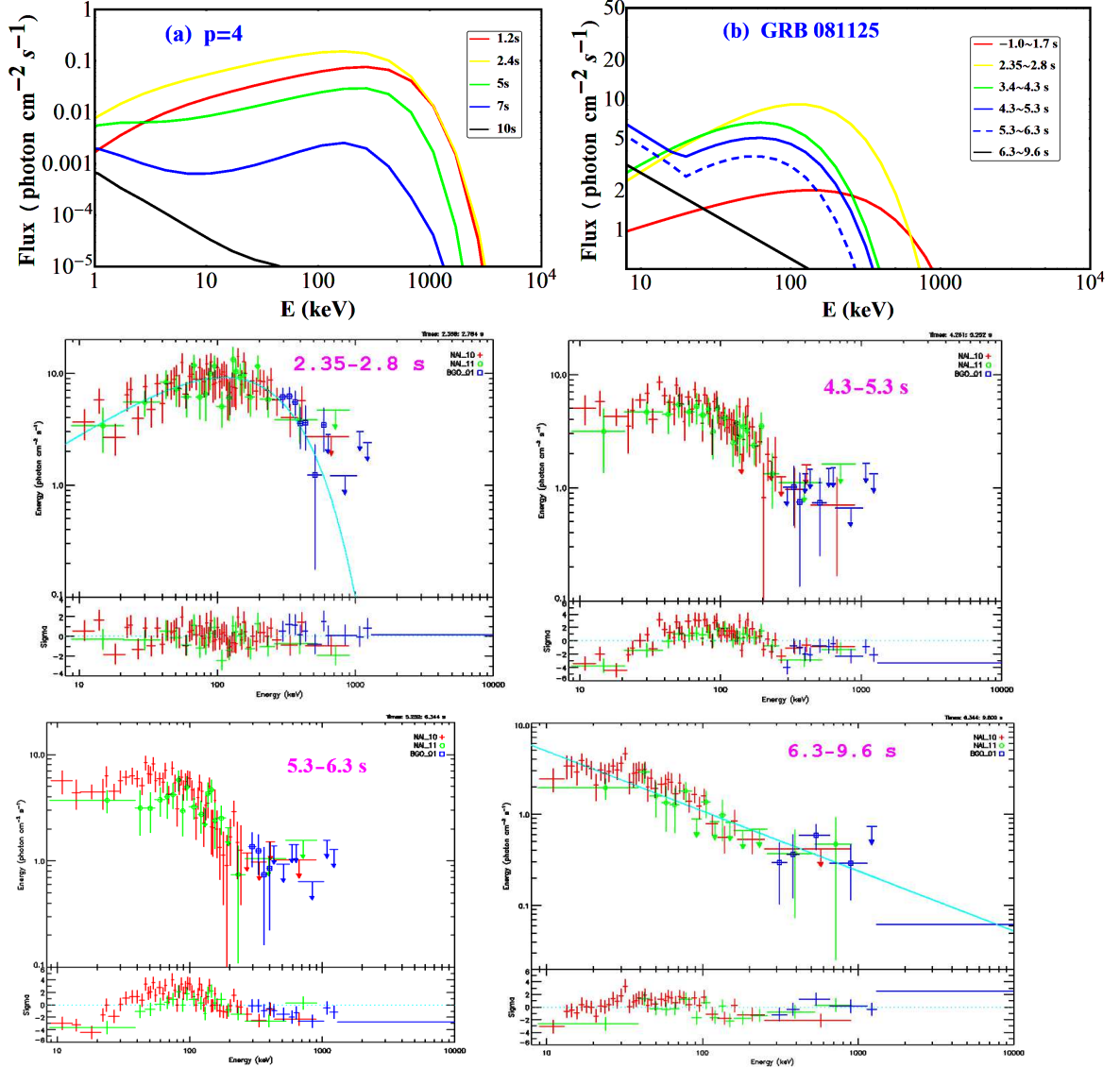


FIG. 10.— Comparison of the calculated time-resolved spectra for $\theta_c \Gamma_0 = 1$, $p = 4$ and the time-resolved spectral analysis results of GRB 081125. Top left panel: the calculated time-resolved spectra for $\theta_c \Gamma_0 = 1$ and $p = 4$, same as Figure 7a. Top right panel: the best-fit model spectra of the time-resolved spectra from GRB 081125 for several different time intervals. Middle and bottom panels: the spectral fits to the time-resolved spectra for 2.35 – 2.8 s (middle left) and 6.3 – 9.6 s (bottom right), and the observed spectra (fitted with the PL model) for 4.3 – 5.3 s (middle right) and 5.3 – 6.3 s (bottom left).

power law with negative index, but the modified blackbody with the flattened shape ($F_\nu \sim \nu^0$) below the peak. The best-fit results of the time-resolved spectra are almost consistent with those of Yu et al. (2016), where the best-fit models before 13.975 s are all the COMP model and the best-fit low-energy spectral index changes from -0.2 to -1 .

Figures 14 and 15 present the time-resolved spectral analysis results of GRB 090809B and GRB 110817A, respectively. The observed spectral evolution for each is similar to that for GRB 081224, thus the case of $\theta_c \Gamma_0 = 10$ and $p = 4$. The best-fit results of the time-resolved spectra are also almost consistent with those of Yu et al. (2016).

According to the above analyses, we can see that the photosphere model with an angular Lorentz factor profile may explain the observed spectral evolution well. In

addition, the observed spectral evolutions for multi-pulse GRBs and single-pulse GRBs seem to be different. The θ_c for multi-pulse GRBs seems to be more narrow, while much wider for the single-pulse GRBs.

3.5. Luminosity profiles and E_p evolution

The light curve is an important observational characteristic for GRBs. Here, in Figure 16, we use the light curve profiles of a few GRBs to test the reasonability of our initial wind luminosity L_w profiles⁶. Also, we explore the parameter dependencies of the photosphere luminosity L_{ph} profiles. For the initial wind luminosity L_w profile of $a_r = 0.75$ and $a_d = -5$, the photosphere luminosity L_{ph} profile (blue triangle points) is close to the light curve profile of GRB 090131B. While for the ini-

⁶ Note that we mainly focus on the decay phase since the time scale for the rise phase is quite short.

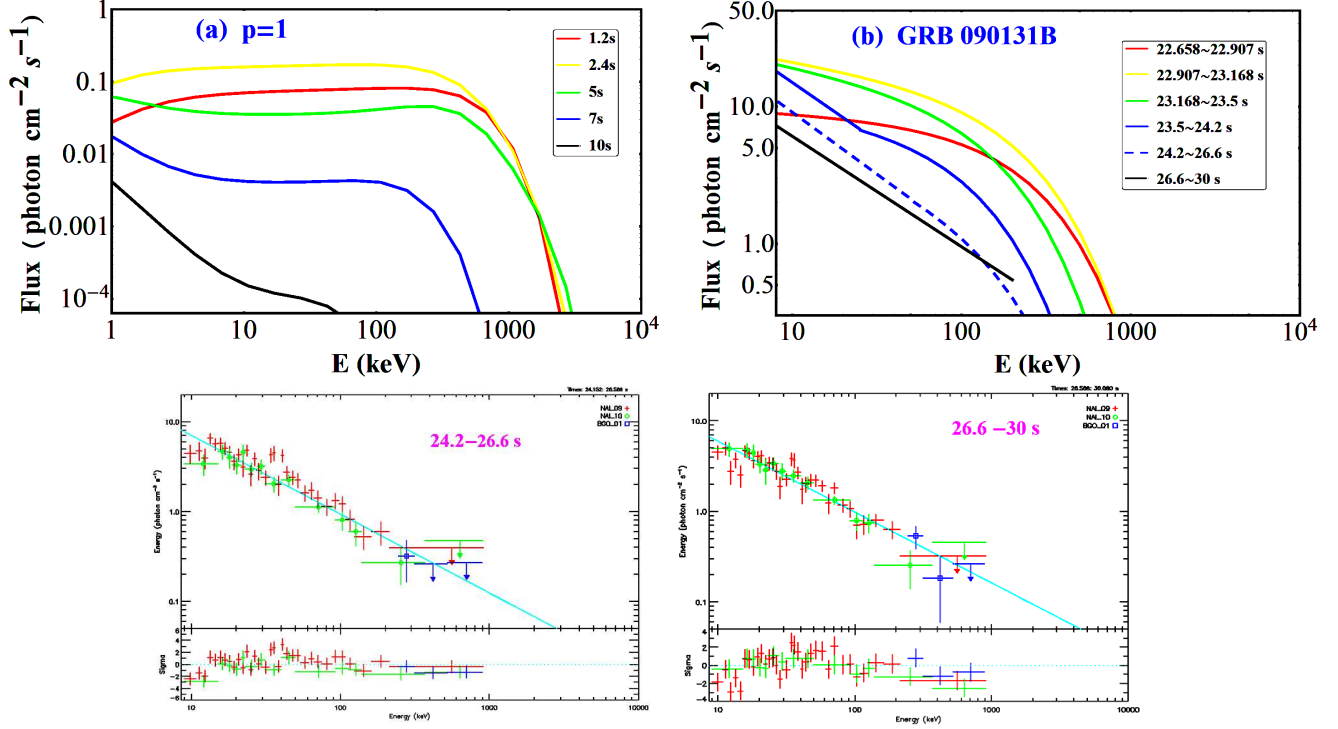


FIG. 11.— Comparison of the calculated time-resolved spectra for $\theta_c \Gamma_0 = 1$, $p = 1$ and the time-resolved spectral analysis results of GRB 090131B. Top left panel: the calculated time-resolved spectra for $\theta_c \Gamma_0 = 1$ and $p = 1$, same as Figure 6c. Top right panel: the best-fit model spectra of the time-resolved spectra from GRB 090131B for several different time intervals. Bottom panels: the spectral fits to the time-resolved spectra for 24.2 – 26.6 s and 26.6 – 30 s (from left to right), respectively.

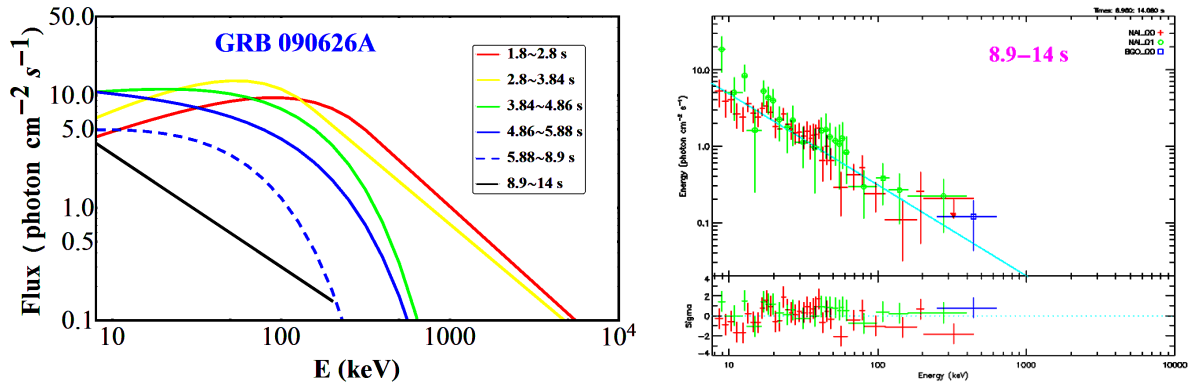


FIG. 12.— The time-resolved spectral analysis results of GRB 090626A. Left panel: the best-fit model spectra of the time-resolved spectra from GRB 090626A for several different time intervals. Right panel: the spectral fits to the time-resolved spectrum for 8.9 – 14 s.

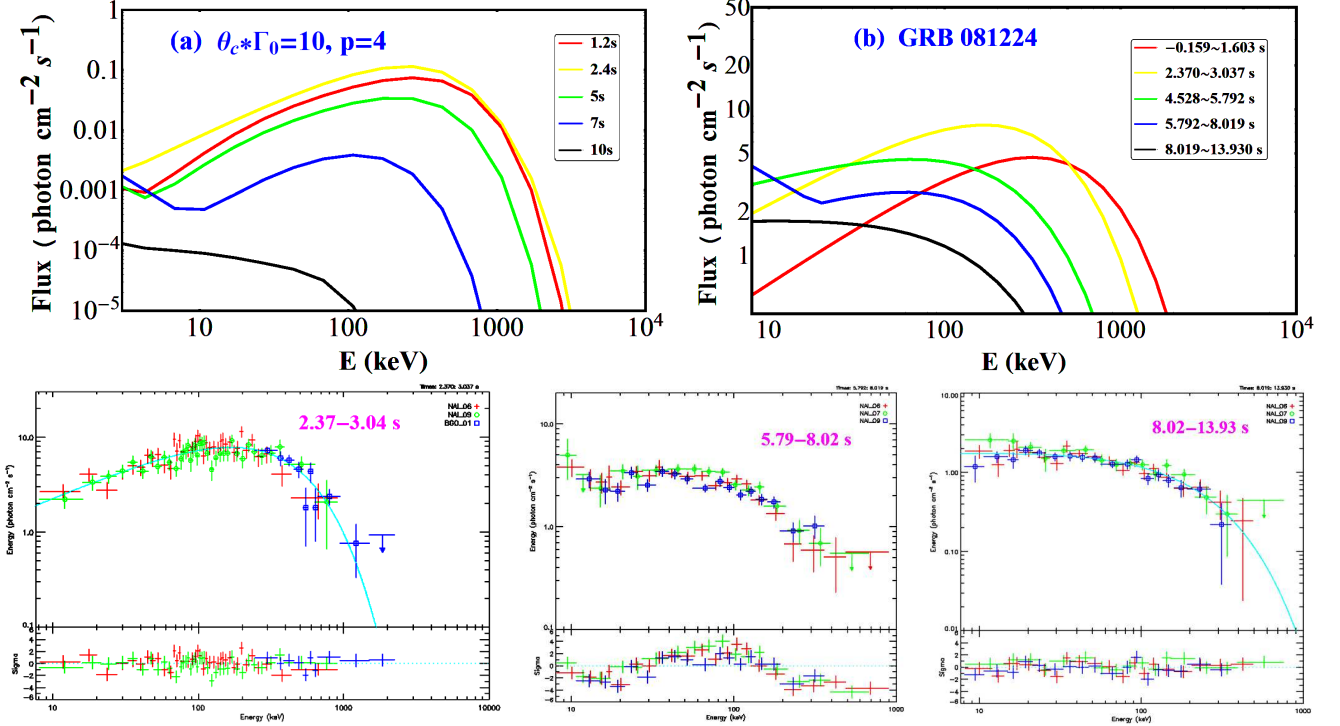


FIG. 13.— Comparison of the calculated time-resolved spectra for $\theta_c \Gamma_0 = 10$, $p = 4$ and the time-resolved spectral analysis results of GRB 081224. Top left panel: the calculated time-resolved spectra for $\theta_c \Gamma_0 = 10$ and $p = 4$, same as Figure 7b. Top right panel: the best-fit model spectra of the time-resolved spectra from GRB 081224 for several different time intervals. Bottom panels: the spectral fits to the time-resolved spectra for 2.370 – 3.037 s (left) and 8.019 – 13.930 s (right), and the observed spectrum (fitted with the PL model) for 5.792 – 8.019 s (middle).

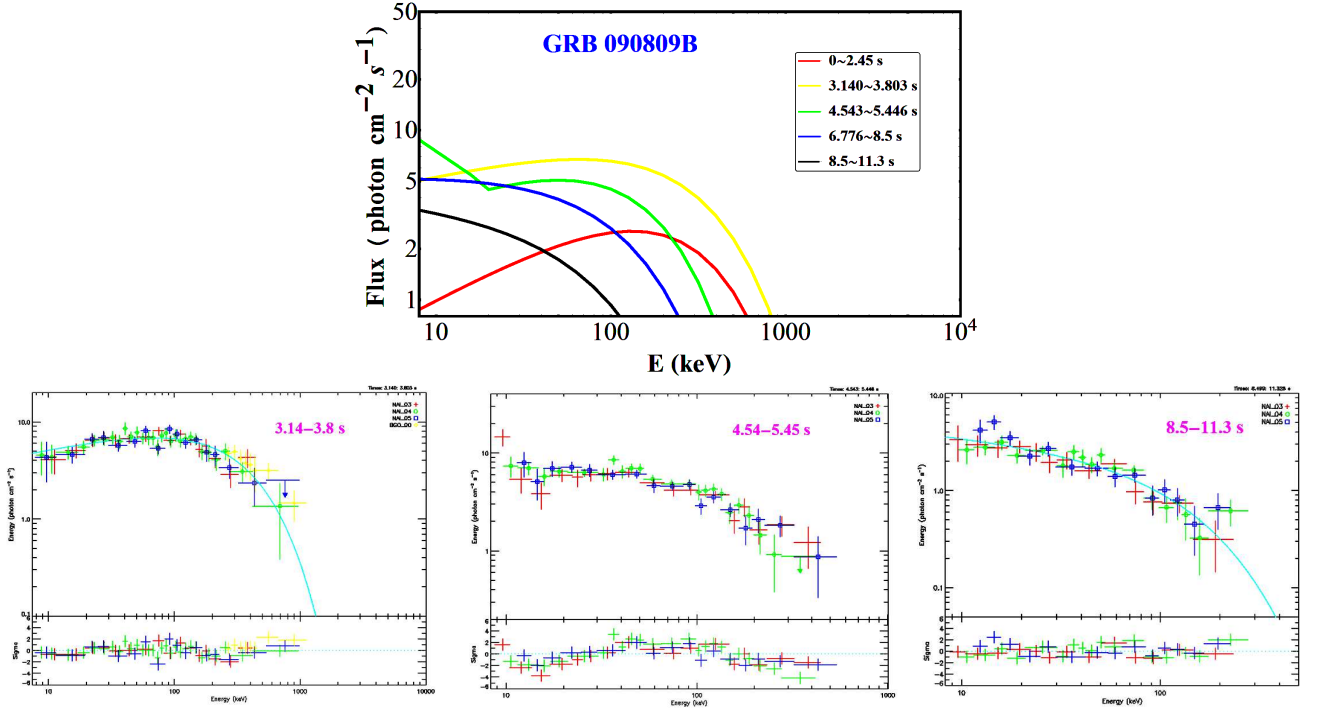


FIG. 14.— The time-resolved spectral analysis results of GRB 090809B. Top panel: the best-fit model spectra of the time-resolved spectra from GRB 090809B for several different time intervals. Bottom panels: the spectral fits to the time-resolved spectra for 3.140 – 3.803 s (left) and 8.5 – 11.3 s (right), and the observed spectrum (fitted with the PL model) for 4.543 – 5.446 s (middle).

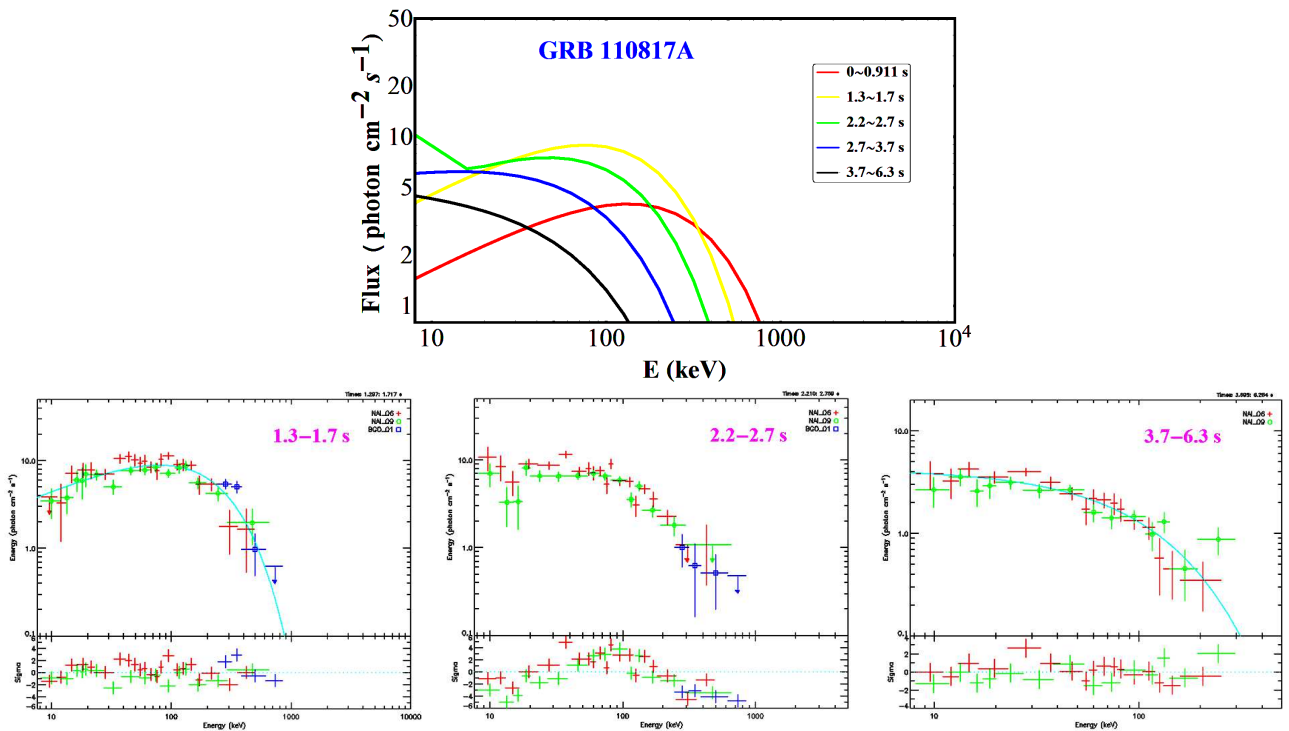


FIG. 15.— The time-resolved spectral analysis results of GRB 110817A. Top panel: the best-fit model spectra of the time-resolved spectra from GRB 110817A for several different time intervals. Bottom panels: the spectral fits to the time-resolved spectra for 1.3 – 1.7 s (left) and 3.7 – 6.3 s (right), and the observed spectrum (fitted with the PL model) for 2.2 – 2.7 s (middle).

tial wind luminosity L_w profile of $\tau_1 = 32$, $\tau_2 = 0.5$ and $\hat{t}_s = -1.6$, the photosphere luminosity L_{ph} profiles (the points of different shapes and colors for various parameters) are close to the light curve profile of GRB 110817A. As for the parameter dependencies, the photosphere luminosity L_{ph} falls down more rapidly for a wider jet core ($\theta_c \Gamma_0 = 10$, $p = 1$ or $\theta_c \Gamma_0 = 10$, $p = 4$) or larger r_0 ($r_0 = 10^9$ cm), and more slowly for a narrower jet core ($\theta_c \Gamma_0 = 1/10$, $p = 0.5$), smaller Γ_0 ($\Gamma_0 = 200$), non-zero viewing angle ($\theta_v = 1/400$ or $\theta_c = 1/40$, $p = 4$, $\theta_v = 1/40$) or larger $L_{w,p}$ ($L_{w,p} = 10^{53}$ erg s $^{-1}$).

Furthermore, the evolution of E_p is crucial to judge whether a GRB prompt emission model is better. Observationally, the hard-to-soft evolution and intensity-tracking patterns have been identified (Ford et al. 1995; Liang & Kargatis 1996; Lu et al. 2010, 2012). For the photosphere emission model of a uniform jet, Deng & Zhang (2014) showed that the observed hard-to-soft evolution pattern cannot be reproduced, and the $E_p - L$ tracking pattern can be reproduced when the dimensionless entropy η depends positively on L_w . Here, by considering the structured jet and including the $R_{\text{ph}} < R_s$ regime, we can reproduce the hard-to-soft evolution and intensity-tracking patterns better with the photosphere model.

Based on the numerical results of the time-resolved spectra presented in Figure 6c ($\theta_c \Gamma_0 = 1$, $p = 1$) and Figure 7b ($\theta_c \Gamma_0 = 10$, $p = 4$), we plot the evolution of E_p with respect to wind luminosity ($\tau_1 = 32$, $\tau_2 = 0.5$, $\hat{t}_s = -1.6$) in the top left panel of Figure 17. An approximate hard-to-soft evolution is shown, except for a slight increase after the peak of L_w . The evolution is similar for other Lorentz factor profiles and viewing angles considered above. Now, we perform some analytical discussions. For the regime $R_{\text{ph}} > R_s$ (relatively large L_w near the peak), the observed temperature can be expressed as

$$\begin{aligned} T_{\text{ph}}(\theta) &\propto L_w^{1/4} r_0^{-1/2} [R_{\text{ph}}(\theta)/R_s(\theta)]^{-2/3} \\ &\propto L_w^{1/4} r_0^{-1/2} \{ [L_w/\Gamma^3(\theta)] / [\Gamma(\theta)r_0] \}^{-2/3} \\ &\propto L_w^{-5/12} r_0^{1/6} \Gamma^{8/3}(\theta). \end{aligned} \quad (27)$$

Here, the observed temperature is angle-dependent. Compared with the case of a uniform jet (black solid line), the $L_w - E_p$ anti-correlation is much weaker. And if we consider the time-integrated spectra, the anti-correlation may almost disappear. Then as the L_w falls down, one enters the regime $R_{\text{ph}} < R_s$, and

$$T_{\text{ph}}(\theta) \propto L_w^{1/4} r_0^{-1/2}. \quad (28)$$

Now, we have $E_p \propto L_w^{1/4}$, which means E_p decreases. Thus, an approximate hard-to-soft evolution shows up. For the time-integrated spectra of the wind luminosity $a_r = 0.75$, $a_d = -5$ which has a steeper decay phase, the hard-to-soft evolution is rather well as showed in the top right panel of Figure 17. For this wind luminosity, the photosphere luminosity L_{ph} in the decay phase has an index of $a_d = -2.5$ which is consistent with the average decay phase index $d = 2.44 \pm 0.12$ of a large sample of GRBs in Kocevski et al. (2003). In addition, with a larger r_0 ($r_0 = 10^9$ cm) the evolution of E_p acts as the intensity-tracking pattern well, as showed in the bottom panel of

Figure 17. This is because the $R_{\text{ph}} < R_s$ regime works for the whole wind profile (For the same reason, the intensity-tracking pattern can be obtained with smaller peak luminosity $L_{w,p} = 10^{51}$ erg s $^{-1}$). And the much larger r_0 is consistent with the rather high mean value $\langle r_0 \rangle \sim 10^{8.5}$ cm deduced in Pe'er et al. (2015).

4. CONCLUSIONS AND DISCUSSION

In this paper, we investigate the time-resolved spectra and E_p evolutions of photospheric emission from a structured jet. To be more realistic, a continuous wind with a time-dependent wind luminosity has been considered. The following conclusions are drawn. (1) The photosphere spectrum near the peak luminosity is similar to the spectrum of the cutoff power-law model, which is the best-fit model for a large percentage of the time-resolved spectra in GRBs (e.g., Kaneko et al. 2006; Yu et al. 2016). (2) The photosphere spectrum near the peak luminosity can have a flattened shape ($F_\nu \sim \nu^0$) below the peak, consistent with the average low-energy spectral index ($\alpha \sim -1$) for the time-resolved spectra observed in GRBs (e.g., Kaneko et al. 2006; Yu et al. 2016). Also, the distribution of the low-energy spectral index for our photosphere model is similar to that observed ($-2 \lesssim \alpha \lesssim 0$). For $\theta_c \Gamma_0 = 1/10$ and $p = 0.5$, $\alpha \sim -1.8$; for $\theta_c \Gamma_0 = 10$ and $p = 4$, $\alpha \sim 0$. (3) Judged by the width of the jet core, the spectral evolutions during the decay phase for our photosphere model can be mainly divided into two types. A power law with negative index gradually emerges for narrower core ($\theta_c \Gamma_0 = 1$), while a modified blackbody with a flattened shape ($F_\nu \sim \nu^0$) below the peak shows up for wider core ($\theta_c \Gamma_0 = 10$, $p = 4$). Based on the time-resolved spectral analysis of several GRBs observed by *Fermi* GBM and possessing a pulse that has a rather good profile, we find that the above-mentioned two kinds of spectral evolutions during the decay phase do seem to exist. The spectral evolution for the multi-pulse GRBs is similar to that for narrower jet core, while the single-pulse GRBs similar to wider jet core. (4) For this photosphere model, we can reproduce the two types of observed E_p evolution patterns rather well. For the typical parameters, we get the hard-to-soft evolution; and for a larger r_0 ($r_0 = 10^9$ cm) or smaller $L_{w,p}$ ($L_{w,p} = 10^{51}$ erg s $^{-1}$), we have the intensity-tracking pattern. From the above, by considering the geometrical broadening for structured jet, we reproduce the observed time-resolved spectra, the spectral evolutions and E_p evolutions well for the GRBs best fitted by the cutoff power-law model for the peak-flux spectrum or the time-integrated spectrum.

Photospheric emission for spherically symmetric outflows has been investigated by several authors (Pe'er 2008; Beloborodov 2011; Pe'er & Ryde 2011; Deng & Zhang 2014). But hydrodynamic simulations for a jet propagating through the envelope of the progenitor star (Zhang, Woosley & MacFadyen 2003; Mizuta et al. 2006; Morsony, Lazzati & Begelman 2007; Lazzati et al. 2009; Nagakura et al. 2011) show that the jet should have lateral structure and rapid time variability. Thus, in this paper we consider an angular Lorentz factor profile and a continuous wind with a time-dependent wind luminosity. Lundman et al. (2013) showed that, with an inner-constant and outer-decreasing angular Lorentz factor profile and steady-state jet, the photospheric spec-

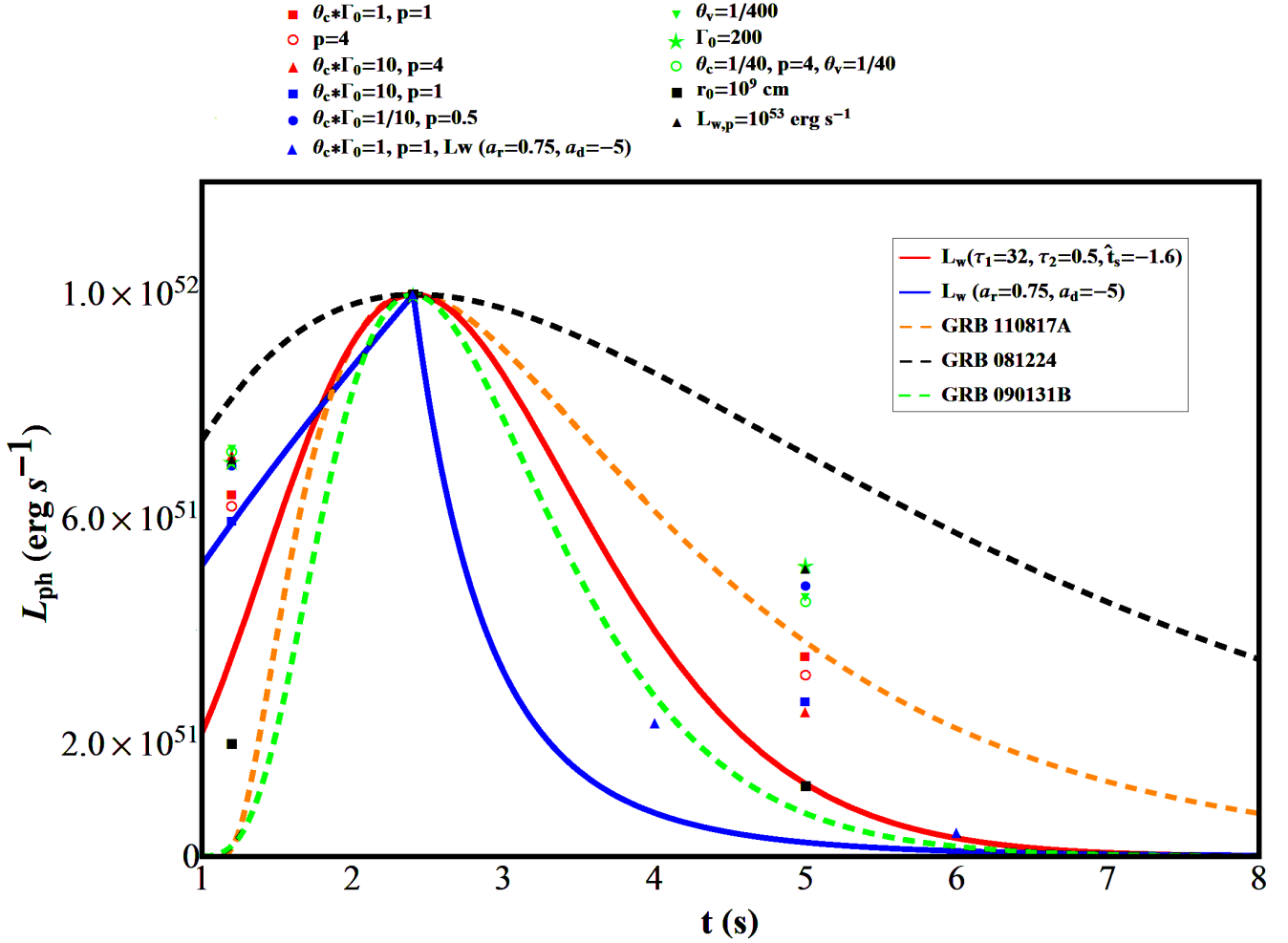


FIG. 16.— The initial wind luminosity L_w and photosphere luminosity L_{ph} profiles. For comparison, the photosphere luminosity L_{ph} profiles have all been normalized to $L_{w,p} = 10^{52} \text{ erg s}^{-1}$ at 2.4 s. The initial wind luminosity L_w profiles for the exponential model ($\tau_1 = 32$, $\tau_2 = 0.5$, $\hat{t}_s = -1.6$) and the broken power law model ($a_r = 0.75$, $a_d = -5$) are plotted by the red solid line and the blue solid line, respectively. The photosphere luminosity L_{ph} profiles for the exponential model with various parameters are shown by the points of different shapes and colors at 1.2 s, 2.4 s and 5 s. While the photosphere luminosity L_{ph} profile for the broken power law model with the typical parameters ($\theta_c \Gamma_0 = 1$, $p = 1$, $\theta_v = 0$) is shown by the blue triangle points at 2.4 s, 4 s and 6 s. The three dashed lines are the light curves for GRB 110817A (orange), GRB 081224 (black) and GRB 090131B (green), respectively.

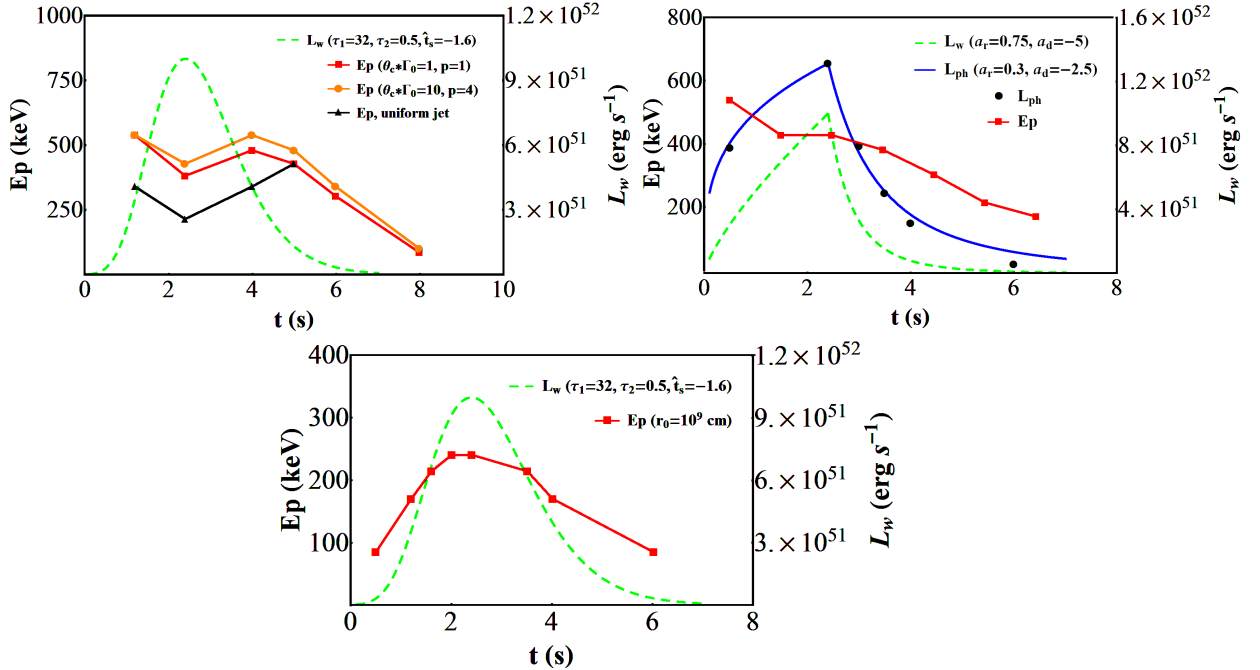


FIG. 17.— Evolution of E_p for different parameters. Top left panel: initial wind luminosity L_w (green dashed line) and evolution of E_p with “ $\theta_c\Gamma_0 = 1$, $p = 1$ ” (red solid line), “ $\theta_c\Gamma_0 = 10$, $p = 4$ ” (orange solid line) or a uniform jet (black solid line) for the case “ $\tau_1 = 32$, $\tau_2 = 0.5$, $\hat{t}_s = -1.6$ ”. Top right panel: E_p evolution (red solid line), the initial wind luminosity L_w (green dashed line) and the photosphere luminosity L_{ph} (black circle points and blue solid line) for the case “ $a_r = 0.75$, $a_d = -5$ ”. The E_p is for the time-integrated spectra here, which have a time bin of 1 s (The E_p at 1.5 s is for the time interval of 1 – 2 s, and so on). Bottom panel: initial wind luminosity L_w (green dashed line) and evolution of E_p with $r_0 = 10^9$ cm (red solid line) for the case “ $\tau_1 = 32$, $\tau_2 = 0.5$, $\hat{t}_s = -1.6$ ”.

trum can reproduce the observed average low-energy photon index $\alpha \approx -1$. But whether the time-resolved spectra, the spectral evolutions and E_p evolutions for more reasonable energy injection of continuous wind can match the observations needs to be further considered, which have been carefully treated in this paper. And we find that they match well for the GRBs best fitted by the cutoff power-law model for the peak-flux spectrum or the time-integrated spectrum. We only give a rough comparison here since we mainly focus on the model calculations, the complete fit to the data with the model will be further explored in future works.

In this work, we assumed a local thermal radiation spectrum for each independently-evolving angular fluid element and ignored the sideways diffusion effect of photons at certain angular distance. The sideways diffusion can cause a smearing out effect on temperature and lead to a non-thermal spectrum due to inverse Compton radiation for jets with $\theta_c \sim 1/\Gamma_0$ (Ito et al 2013, Lundman et al 2013). Such effect unfortunately can not be calculated by the approach in this paper. We thus caution the spectral calculations performed in this paper when $\theta_c \sim 1/\Gamma_0$, and especially when $\theta_c \ll 1/\Gamma_0$.

In addition, we consider non-dissipative fireball dynamics here. The radial distributions of the Lorentz factor and the comoving temperature in dissipative outflows are significantly different (Giannios 2012; Beloborodov 2013). Energy dissipation in the area of moderate optical depth has been proposed by many authors, with various dissipative mechanisms such as shocks (Pe’er et al. 2005, 2006; Lazzati & Begelman 2010), magnetic re-

connection (Giannios 2006; Giannios & Spruit 2007; Beniamini & Giannios 2017) and proton-neutron nuclear collisions (Beloborodov 2010; Vurm et al. 2011). Then, relativistic electrons are generated that upscatter the thermal photons to shape the non-thermal spectrum above the peak energy. Namely, we may get the Band function spectrum with the observed low-energy photon index if the subphotospheric dissipation and the geometric broadening (for structured jet) coexist. So, decided by whether the dissipation exists, we may obtain the two kinds of spectra (COMP or Band) for the peak-flux spectrum or the time-integrated spectrum within the framework of the photosphere model.

We thank the referee for helpful suggestions. We thank Wei Deng for the helpful discussions. We acknowledge the use of the public data from the *Fermi* data archives. This work is partially supported by the National Natural Science Foundation of China (grant Nos. 11603076, 11673068, 11725314, and U1831122), the Youth Innovation Promotion Association (2017366), the Key Research Program of Frontier Sciences (grant No. QYZDB-S5W-SYS005), the Strategic Priority Research Program “Multi-waveband gravitational wave Universe” (grant No. XDB23000000) of Chinese Academy of Sciences, and the “333 Project” and the Natural Science Foundation (grant No. BK20161096) of Jiangsu Province. B.B.Z. acknowledge the support from the National Thousand Young Talents program of China.

REFERENCES

- Acuner, Z., & Ryde, F. 2018, *MNRAS*, 475, 1708
- Ai, S., Gao, H., Dai, Z.-G., et al. 2018, *ApJ*, 860, 57
- Axelsson, M., Baldini, L., Barbiellini, G., et al. 2012, *ApJL*, 757, L31
- Axelsson, M., & Borgonovo, L. 2015, *MNRAS*, 447, 3150
- Band, D., Matteson, J., Ford, L., et al. 1993, *ApJ*, 413, 281
- Bégué, D., & Pe'er, A. 2015, *ApJ*, 802, 134
- Beloborodov, A. M. 2010, *MNRAS*, 407, 1033
- Beloborodov, A. M. 2011, *ApJ*, 737, 68
- Beloborodov, A. M. 2013, *ApJ*, 764, 157
- Beloborodov, A. M. 2017, *ApJ*, 838, 125
- Beniamini, P., Nava, L., Duran, R. B., & Piran, T. 2015, *MNRAS*, 454, 1073
- Beniamini, P., & Giannios, D. 2017, *MNRAS*, 468, 3202
- Beniamini, P., & Nakar, E. 2019, *MNRAS*, 482, 5430
- Beniamini, P., Petropoulou, M., Barniol Duran, R., & Giannios, D. 2019, *MNRAS*, 483, 840
- Crider, A., Liang, E. P., Smith, I. A., et al. 1997, *ApJL*, 479, L39
- Dai, Z. G., & Gou, L. J. 2001, *ApJ*, 552, 72
- Deng, W., & Zhang, B. 2014, *ApJ*, 785, 112
- Fan, Y., & Piran, T. 2006, *MNRAS*, 369, 197
- Fan, Y.-Z., Wei, D.-M., Zhang, F.-W., & Zhang, B.-B. 2012, *ApJL*, 755, L6
- Ford, L. A., Band, D. L., Matteson, J. L., et al. 1995, *ApJ*, 439, 307
- Gao, H., & Zhang, B. 2015, *ApJ*, 801, 103
- Geng, J.-J., Huang, Y.-F., Wu, X.-F., Zhang, B., & Zong, H.-S. 2018a, *ApJS*, 234, 3
- Geng, J.-J., Dai, Z.-G., Huang, Y.-F., et al. 2018b, *ApJ*, 856, L33
- Geng, J.-J., Zhang, B., Kölligan, A., Kuiper, R., & Huang, Y.-F. 2019, *ApJ*, 877, L40
- Ghirlanda, G., Nava, L., & Ghisellini, G. 2010, *A&A*, 511, A43
- Ghirlanda, G., Pescalli, A., & Ghisellini, G. 2013, *MNRAS*, 432, 3237
- Ghirlanda, G., Salafia, O. S., Paragi, Z., et al. 2019, *Science*, 363, 968
- Giannios, D. 2006, *A&A*, 457, 763
- Giannios, D., & Spruit, H. C. 2007, *A&A*, 469, 1
- Giannios, D. 2012, *MNRAS*, 422, 3092
- Goldstein, A., Burgess, J. M., Preece, R. D., et al. 2012, *ApJS*, 199, 19
- Goodman, J. 1986, *ApJL*, 308, L47
- Guetta, D., Spada, M., & Waxman, E. 2001, *ApJ*, 557, 399
- Guiriec, S., Daigne, F., Hascoët, R., et al. 2013, *ApJ*, 770, 32
- Guiriec, S., Connaughton, V., Briggs, M. S., et al. 2011, *ApJL*, 727, L33
- Hou, S.-J., Zhang, B.-B., Meng, Y.-Z., et al. 2018, *ApJ*, 866, 13
- Ito, H., Nagataki, S., Ono, M., et al. 2013, *ApJ*, 777, 62
- Kaneko, Y., Preece, R. D., Briggs, M. S., et al. 2006, *ApJS*, 166, 298
- Kino, M., Mizuta, A., & Yamada, S. 2004, *ApJ*, 611, 1021
- Kobayashi, S., Piran, T., & Sari, R. 1997, *ApJ*, 490, 92
- Kocevski, D., Ryde, F., & Liang, E. 2003, *ApJ*, 596, 389
- Lan, M.-X., Geng, J.-J., Wu, X.-F., & Dai, Z.-G. 2019, *ApJ*, 870, 96
- Larsson, J., Racusin, J. L., & Burgess, J. M. 2015, *ApJL*, 800, L34
- Lazzati, D., Ghisellini, G., & Celotti, A. 1999, *MNRAS*, 309, L13
- Lazzati, D., Morsony, B. J., & Begelman, M. C. 2009, *ApJL*, 700, L47
- Lazzati, D., & Begelman, M. C. 2010, *ApJ*, 725, 1137
- Lazzati, D., Morsony, B. J., Margutti, R., & Begelman, M. C. 2013, *ApJ*, 765, 103
- Lazzati, D., Perna, R., Morsony, B. J., et al. 2018, *Physical Review Letters*, 120, 241103
- Li, B., Li, L.-B., Huang, Y.-F., et al. 2018, *ApJ*, 859, L3
- Li, L. 2019, *ApJS*, 242, 16
- Li, L. 2019, arXiv:1905.02340
- Li, L.-B., Geng, J.-J., Huang, Y.-F., & Li, B. 2019, arXiv:1901.08266
- Liang, E., & Kargatis, V. 1996, *Nature*, 381, 49
- Lin, D.-B., Liu, T., Lin, J., et al. 2018, *ApJ*, 856, 90
- Lu, R.-J., Hou, S.-J., & Liang, E.-W. 2010, *ApJ*, 720, 1146
- Lu, R.-J., Wei, J.-J., Liang, E.-W., et al. 2012, *ApJ*, 756, 112
- Lundman, C., Pe'er, A., & Ryde, F. 2013, *MNRAS*, 428, 2430
- Lü, H.-J., Lü, J., Zhong, S.-Q., et al. 2017, *ApJ*, 849, 71
- Lyman, J. D., Lamb, G. P., Levan, A. J., et al. 2018, *Nature Astronomy*, 2, 751
- MacFadyen, A. I., & Woosley, S. E. 1999, *ApJ*, 524, 262
- Meng, Y.-Z., Geng, J.-J., Zhang, B.-B., et al. 2018, *ApJ*, 860, 72
- Mészáros, P., & Rees, M. J. 2000, *ApJ*, 530, 292
- Mizuta, A., Yamasaki, T., Nagataki, S., & Mineshige, S. 2006, *ApJ*, 651, 960
- Mizuta, A., Nagataki, S., & Aoi, J. 2011, *ApJ*, 732, 26
- Mooley, K. P., Deller, A. T., Gottlieb, O., et al. 2018, *Nature*, 561, 355
- Morsony, B. J., Lazzati, D., & Begelman, M. C. 2007, *ApJ*, 665, 569
- Nagakura, H., Ito, H., Kiuchi, K., & Yamada, S. 2011, *ApJ*, 731, 80
- Nava, L., Ghirlanda, G., Ghisellini, G., & Celotti, A. 2011, *A&A*, 530, A21
- Norris, J. P., Bonnell, J. T., Kazanas, D., et al. 2005, *ApJ*, 627, 324
- Paczynski, B. 1986, *ApJL*, 308, L43
- Pe'er, A., Mészáros, P., & Rees, M. J. 2005, *ApJ*, 635, 476
- Pe'er, A., Mészáros, P., & Rees, M. J. 2006, *ApJ*, 642, 995
- Pe'er, A. 2008, *ApJ*, 682, 463
- Pe'er, A., & Ryde, F. 2011, *ApJ*, 732, 49
- Pe'er, A., Barlow, H., O'Mahony, S., et al. 2015, *ApJ*, 813, 127
- Pescalli, A., Ghirlanda, G., Salvaterra, R., et al. 2016, *A&A*, 587, A40
- Piran, T. 1999, *Phys. Rep.*, 314, 575
- Preece, R. D., Briggs, M. S., Mallozzi, R. S., et al. 1998, *ApJL*, 506, L23
- Preece, R. D., Briggs, M. S., Mallozzi, R. S., et al. 2000, *ApJS*, 126, 19
- Rees, M. J., & Meszaros, P. 1994, *ApJL*, 430, L93
- Rees, M. J., & Mészáros, P. 2005, *ApJ*, 628, 847
- Rossi, E., Lazzati, D., & Rees, M. J. 2002, *MNRAS*, 332, 945
- Ruffini, R., Siutsou, I. A., & Vereshchagin, G. V. 2013, *ApJ*, 772, 11
- Ryde, F. 2004, *ApJ*, 614, 827
- Ryde, F. 2005, *ApJL*, 625, L95
- Ryde, F., & Pe'er, A. 2009, *ApJ*, 702, 1211
- Ryde, F., Axelsson, M., Zhang, B. B., et al. 2010, *ApJL*, 709, L172
- Ryde, F., Lundman, C., & Acuner, Z. 2017, *MNRAS*, 472, 1897
- Thompson, C. 1994, *MNRAS*, 270, 480
- Toma, K., Wu, X.-F., & Mészáros, P. 2011, *MNRAS*, 415, 1663
- Vurm, I., Beloborodov, A. M., & Poutanen, J. 2011, *ApJ*, 738, 77
- Vurm, I., & Beloborodov, A. M. 2016, *ApJ*, 831, 175
- Wang, Y.-Z., Shao, D.-S., Jiang, J.-L., et al. 2019, *ApJ*, 877, 2
- Wei, J.-J., Zhang, B.-B., Shao, L., Wu, X.-F., & Mészáros, P. 2017, *ApJ*, 834, L13
- Yu, H.-F., van Eerten, H. J., Greiner, J., et al. 2015, *A&A*, 583, A129
- Yu, H.-F., Preece, R. D., Greiner, J., et al. 2016, *A&A*, 588, A135
- Yu, H.-F., Dereli-Bégué, H., & Ryde, F. 2018, arXiv:1810.07313
- Zhang, B.-B., Zhang, B., Liang, E.-W., et al. 2011, *ApJ*, 730, 141
- Zhang, B.-B., Zhang, B., Castro-Tirado, A. J., et al. 2018a, *Nature Astronomy*, 2, 69
- Zhang, B.-B., Zhang, B., Sun, H., et al. 2018b, *Nature Communications*, 9, 447
- Zhang, B., & Mészáros, P. 2002, *ApJ*, 581, 1236
- Zhang, B., Dai, X., Lloyd-Ronning, N. M., & Mészáros, P. 2004, *ApJL*, 601, L119
- Zhang, B., Liang, E., Page, K. L., et al. 2007, *ApJ*, 655, 989
- Zhang, B. 2011, *Comptes Rendus Physique*, 12, 206
- Zhang, B., & Yan, H. 2011, *ApJ*, 726, 90
- Zhang, W., Woosley, S. E., & MacFadyen, A. I. 2003, *ApJ*, 586, 356